Journal of Wind Engineering & Industrial Aerodynamics 201 (2020) 104178

Contents lists available at ScienceDirect

Journal of Wind Engineering & Industrial Aerodynamics

journal homepage: www.elsevier.com/locate/jweia

Large eddy simulations of slope effects on flow fields over isolated hills and ridges

Zhenqing Liu [a,*], Wei Wang [b], Yize Wang [a], Takeshi Ishihara [c]

[a] Institute of Computational Wind Engineering and Wind Energy, School of Civil Engineering & Mechanics, Huazhong University of Science and Technology, Wuhan, Hubei, China

[b] Department of Architecture and Building Engineering, Tokyo Institute of Technology, Yokohama, Kanagawa, Japan

[c] Department of Civil Engineering, School of Engineering, The University of Tokyo, Tokyo, Japan

ARTICLE INFO

Keywords:
Numerical simulations
LES
Turbulent flow fields
3D hill
2D ridge
Slope

ABSTRACT

The slope of a hill could affect the flow patterns significantly. In the present study, three smooth three dimensional (3D) hills (H2, H4, and H8) and three smooth two dimensional (2D) ridges (R2, R4, and R8), with the hill heights increased by factors of 2.0 while the hill radii are kept constant to achieve different slopes, are examined systematically using large eddy simulations (LES). The reattachment of the flow is found to become difficult as the slope increases or as the shape changes from 3D hill to 2D ridge. In addition, the differences of the flow fields between the 3D hills and the 2D ridges will become more evident as the slope increases. Moreover, the mean velocities and the fluctuations for H2 and R2 are almost the same, whereas as the hill slope increases, the differences between the 3D hills and 2D ridges become stronger, and the similarities between the 3D hills and 2D ridges almost disappear for H8 and R8. Based on information available from LES, an analytical model to predict the fractional speed-up ratio is proposed. As for the turbulence structures over the 3D hills, a spiral structure is identified, and the pitch of the spiral becomes narrow as the hill slope increases. When the hill slope further increases to H8, the spiral structures are broken into separated circular tubes. For R4, a hairpin structure is identified, whereas for R8, the hairpin structure disappears, and a vortex with a long spanwise size occurs periodically.

1. Introduction

Turbulent flow fields over complex terrains have attracted a great deal of interest for a variety of different applications, such as the prediction of pollution diffusion, prediction of forest fire propagation, identification of potential locations of wind turbines, and estimation of wind loads on buildings or bridges. Compared with flows over flat terrains, flows over complex terrains are characterized by large-scale pressure gradients due to the topography, which induces a distortion of the mean flow and generates specific turbulent eddies.

As a starting point to predicting flow fields over real complex terrains, many researches have been conducted to study flows over isolated hills. These researches can be divided into the following: wind tunnel experiments (Gong and Ibbetson, 1989; Ferreira et al., 1995; Kim et al., 1997; Neff and Meroney, 1998; Ishihara et al., 1999; Carpenter and Locke, 1999; Takahashi et al., 2002, 2005; Cao and Tamura, 2006, 2007; Lubitz and White, 2007, etc.), water tunnel experiments (Hunt and Snyder, 1980; Loureiro et al., 2007a, 2007b; 2008), numerical simulations (Kobayashi et al., 1994, Ferreira et al., 1995, Apsley and Castro, 1997, Kim et al., 1997, Uchida and Ohya, 1997, Ishihara and Hibi, 2000, Kim et al., 2001, Iizuka and Kondo, 2004, 2006; Loureiro et al., 2008; Paiva et al., 2009; Mello and Yanagihara, 2010; Griffiths and Middleton, 2010; Balogh et al., 2012; Cao et al., 2012; Pieterse and Harms, 2013; Balogh and Parente, 2015; Liu et al., 2016a, 2016b; Ma and Liu, 2017; Chang et al., 2018, etc.), and field measurements (Salmon et al., 1988; Mickle et al., 1988; Coppin et al., 1994).

The models of isolated hills examined experimentally were primarily 2D ridges and 3D hills with cosine-squared cross sections. A multitude of effects created on flow fields over 2D ridges have been explored. Carpenter and Locke (1999) examined flow fields over multiple 2D ridges, and mean wind speeds over the downstream 2D ridges were found to be decreased because of the wake effects of the upstream 2D ridges. Roughness effects, including sudden changes in roughness conditions, were then investigated in detail by Takahashi et al. (2002) and by Cao

* Corresponding author.
E-mail address: liuzhenqing@hust.edu.cn (Z. Liu).

https://doi.org/10.1016/j.jweia.2020.104178
Received 24 April 2019; Received in revised form 30 March 2020; Accepted 31 March 2020
Available online xxxx
0167-6105/

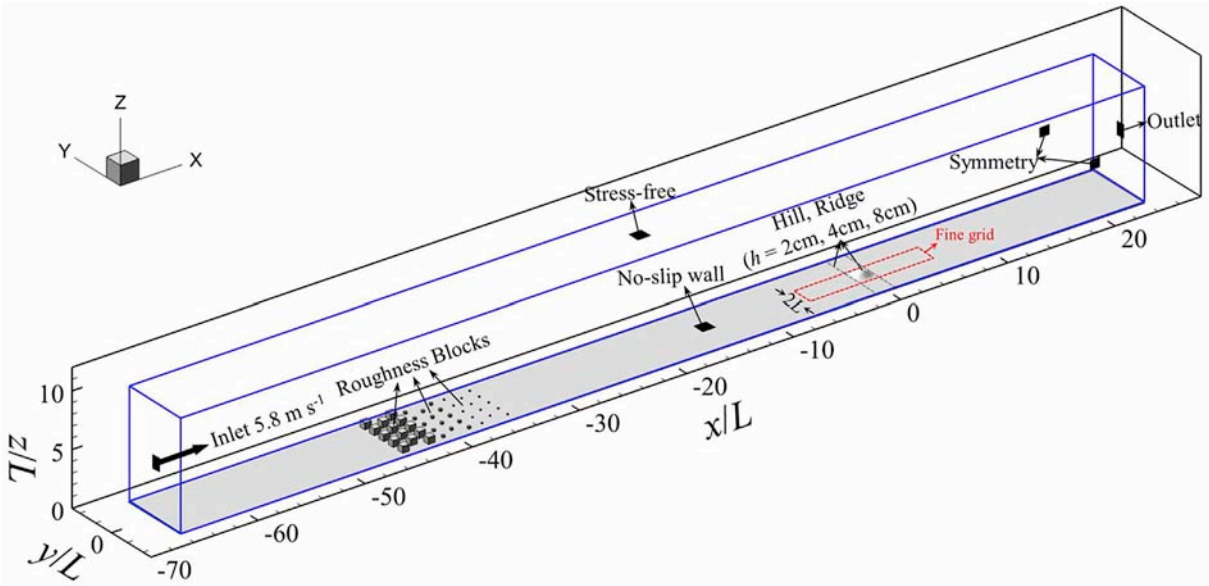

Fig. 1. Configurations of the numerical model.

Table 1
Case settings.

Case name	Radius (mm) L	Heights (mm) h	Maximum Slope S_{max}
H0 (in the absence of hills)	/	/	
H2	100	20	0.32
H4	100	40	0.63
H8	100	80	1.26
R2	100	20	0.32
R4	100	40	0.63
R8	100	80	1.26

and Tamura (2006, 2007). They concluded that roughness on a hill surface or an upstream ground would be significantly impactful on the speed-up ratio over the hill, and that the separation bubble of a rough hill would extend further downstream compared with that of a smooth hill. In addition, Lubitz and White (2007) examined the effect exerted by local wind direction on the speed-up over a 2D ridge and observed that the speed-up would vary considerably when the approaching wind direction was changed. More recently, Li et al. (2017) performed an experimental study on flows over 2D multiple hills with consideration of the effects of the relative heights of the multiple hills.

Nevertheless, because flows over 3D hills are far more complicated than those over 2D ridges, quite a few experiments have been conducted on 3D hills. Gong and Ibbetson (1989) measured flows over 3D hills and 2D ridges, and the results of their study suggested that the mean flow and turbulence are broadly similar, but the perturbation amplitudes for the 3D hills will be reduced. Ishihara et al. (1999) then investigated flow fields over a 3D hill using split-fiber probes designed specifically for the measurement of flows with high turbulence and separations. In their study, pronounced speed-ups at the hilltop and the midway sides were observed.

Given its capabilities to obtain full information about flow fields, computational fluids dynamics (CFD) has been extensively adopted to model flows over various topographies. CFD methods could be split into two major approaches, namely the Reynolds Averaged Navier–Stokes (RANS) method and LES.

With regard to the RANS methods, two-equation models have been widely applied, and among these methods, the performance of an isotropic eddy-viscosity k-ε extension model (Kobayashi et al., 1994), a modified low-Reynolds number k-ε model (Ferreira et al., 1995), standard k-ε model [Kim et al., 1997, Kim, et al., 2001, Ishihara and Hibi, 2000; Loureiro et al., 2008; Mello and Yanagihara, 2010; Griffiths and Middleton, 2010; Chang et al., 2018], isotropization-of-production model (IPM) (Sajjadi et al., 2001), Shih and Durbin models (Lun et al., 2003), renormalization group (RNG)-ε model (Loureiro et al., 2008), and

Fig. 2. Photo of a wind farm in the eastern part of China.

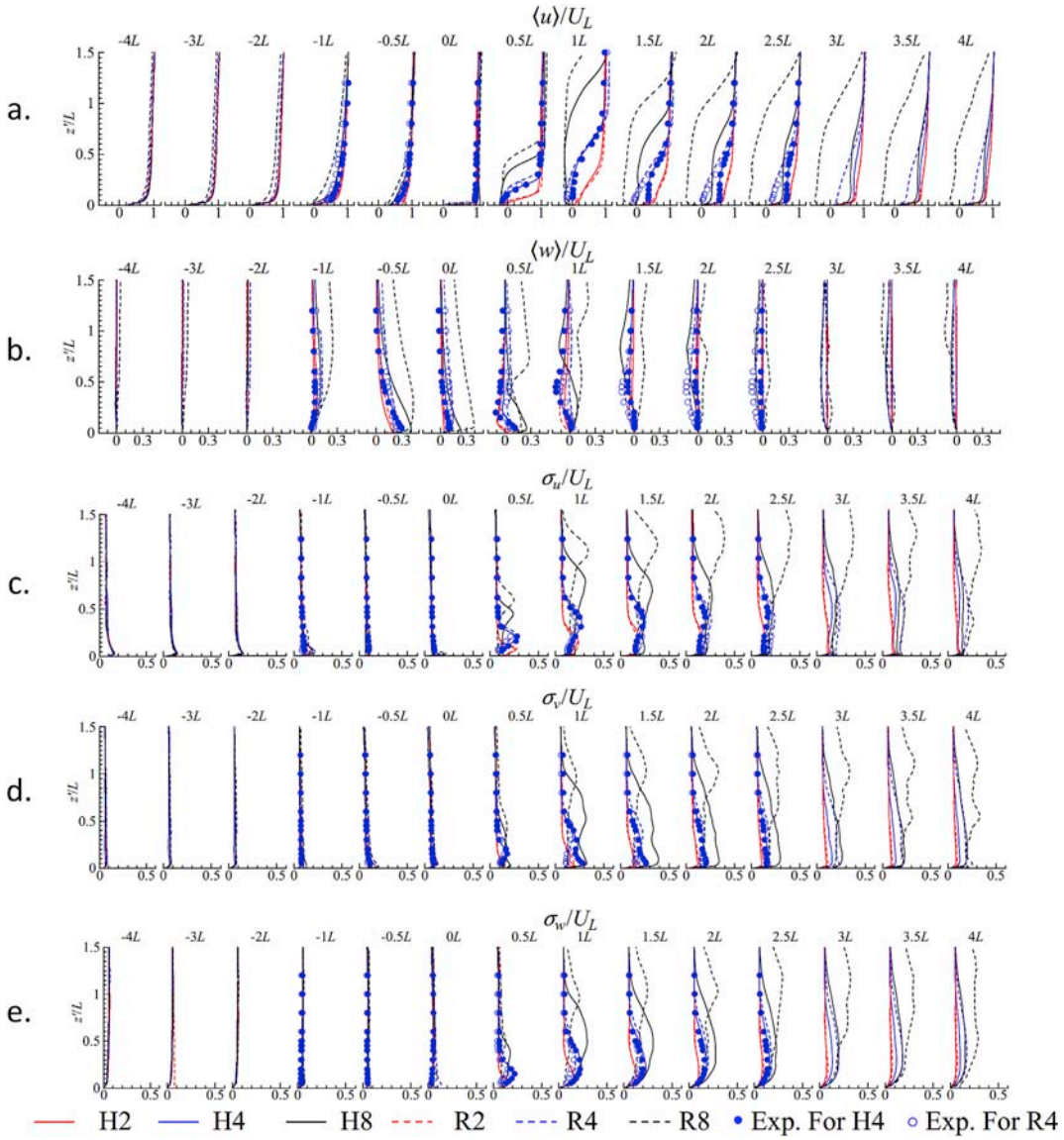

Fig. 3. Vertical mean profiles of (a) streamwise component, u/UL, (b) vertical component, w/UL, and fluctuations of (c) streamwise component, σ_u/U_L, (d) spanwise component, σ_v/U_L, and (e) vertical component, σ_w/U_L.

k–ω models (Loureiro et al., 2008; Hu et al., 2016; Chang et al., 2018) have already been examined. However, RANS methods are incapable of predicting flow fields in wakes very well. Besides, even though instantaneous fields can be obtained via unsteady RANS (URANS), instantaneous structures of turbulence cannot be examined via URANS.

Large eddy simulations, on the other hand, can provide more detailed information in space and time. Iizuka and Kondo (2004, 2006) examined multiple subgrid scale (SGS) models, including standard Smagorinsky model (Smagorinsky, 1963), dynamic Smagorinsky model (Germano et al., 1991), Lagrangian dynamic Smagorinsky model (Meneveau et al., 1996), hybrid (SGS) model (Iizuka and Kondo, 2004), and three variants of Smagorinsky model [I0 (Inagaki et al., 2005), I1 (Iizuka and Kondo, 2006), and I2 (Iizuka and Kondo, 2006)], and suggested that among these the best model is I0, which models the SGS stress using the scale-similarity concept. The large eddy simulations performed by Tamura et al. (2007a, 2007b) showed high accuracies for hills with and without vegetation on the ground when the slopes of the hills were moderate. Cao et al. (2012) and Liu et al. (2016a, 2016b) adopted the standard Smagorinsky SGS model, the results of which revealed excellent consistency with their experiments. More recently, a scale-dependent Lagrangian dynamic model demonstrated excellent performance in the study conducted by Ma and Liu (2017), who discovered that a high horizontal grid resolution was effective for improving the results behind the hill, and that a high vertical grid resolution was capable of improving the results on the lee side of the hill. However, the skewness and kurtosis, as two crucial parameters for estimating peak velocities, and the correlations, which are significant to the estimation of turbulence structures, are rarely studied.

The slope of a hill can affect the flow pattern over the hill significantly. As the hill slope increases, the separation region is expanded, as reported by Kobayashi et al. (1994), Ferreira et al. (1995), Kim et al. (1997), Neff and Meroney (1998), Carpenter and Locke (1999), etc. Moreover, the speed-up ratio rises with the increase in the hill slope, as suggested by Kim, et al. (2001) and Cao et al. (2012). Furthermore, the results obtained by Tamura et al. (2007a,b) demonstrated that the interaction between the incoming turbulence and the shear layer for hills with gentle slopes was not as active as that for hills with steep slopes. However, all of the aforementioned researches that considered the slope effects were restricted to 2D ridges. To our best knowledge, the slope effects on the flow over a 3D hill and the difference with the slope effects over a 2D ridge have been seldom studied.

In the present study, LES is adopted to examine the flow fields over

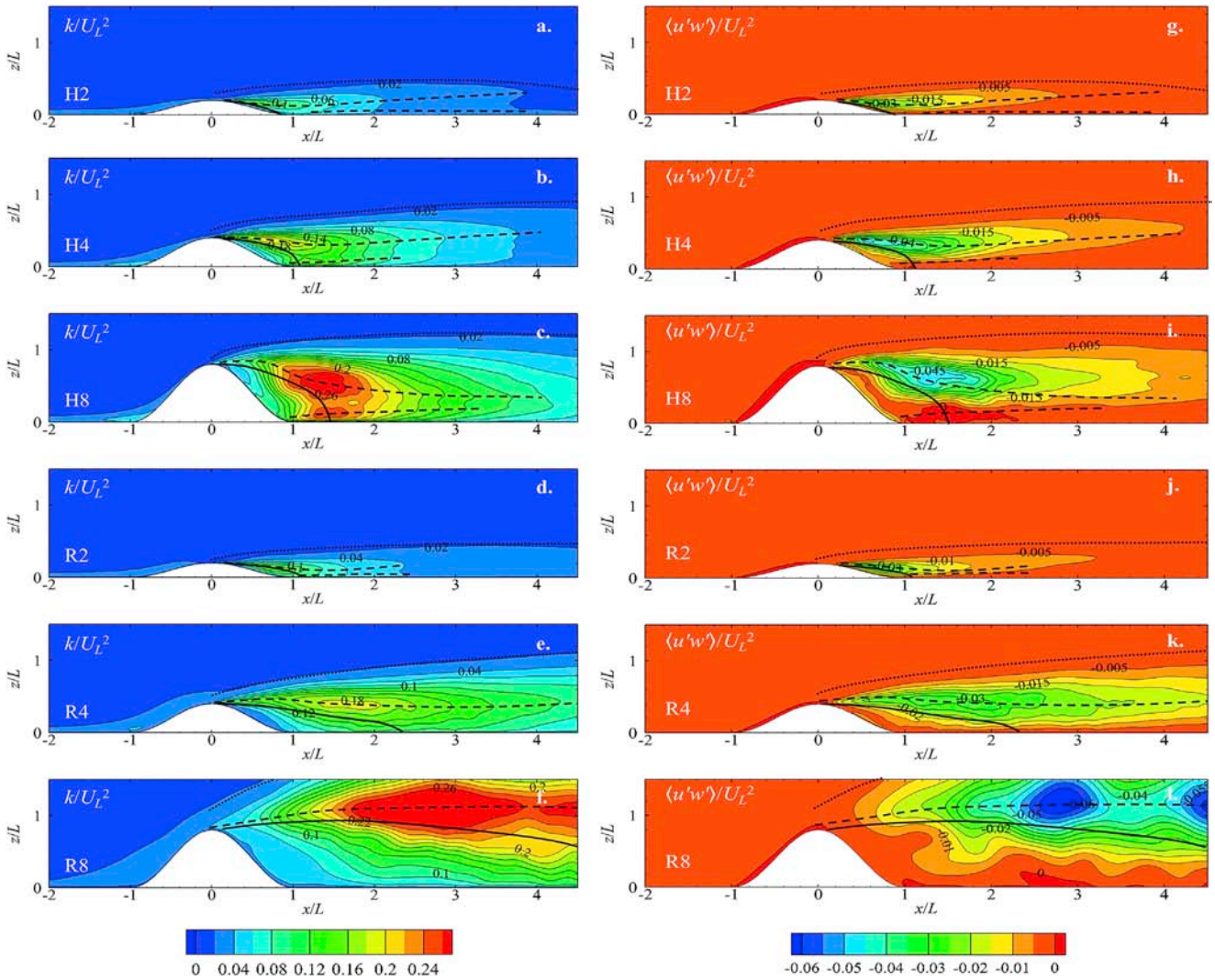

Fig. 4. Distributions of TKE for (a) H2, (b) H4, (c) H8, (d) R2, (e) R4, (f) R8, and u'w' for (g) H2, (h) H4, (i) H8, (j) R2, (k) R4, (l) R8, on the vertical slice of $y = 0$. The dotted lines denote the boundary of the wake depth, the dashed lines indicate the locations of peak TKE, and the solid lines show the center of the separation bubble with zero mean streamwise velocities.

three 3D hills and three 2D ridges with varying slopes. Systematical examinations of the averaged values, e.g., the mean velocity, root mean square (r.m.s.) of the velocity fluctuations, turbulence kinetic energy (TKE), vertical momentum flux, skewness, kurtosis, correlations, and spectrum, are also conducted. Furthermore, the turbulence structures in the wakes are visualized via Q-criteria.

2. Numerical model

2.1. Configurations and mesh system

The numerical model is shown in Fig. 1, where x, y, and z denote the streamwise, spanwise, and vertical directions, respectively. The hills and ridges are placed at (0, 0, 0). The shapes of the 3D hills are determined by

$$\begin{cases} z_s(x,\ y) = h\cos^2\pi\left(x^2 + y^2\right)^{1/2}\Big/2L, & if\ \left(x^2 + y^2\right)^{1/2} < L \\ z_s(x,\ y) = 0, & if\ \left(x^2 + y^2\right)^{1/2} \geq L \end{cases} \quad (1)$$

where L is a constant equal to 100 mm, and h = 20 mm (H2), 40 mm (H4), or 80 mm (H8). The shapes of the ridges are determined by

$$\begin{cases} z_s(x,\ y) = h\cos^2\pi|x|/2L, & if\ |x| < L \\ z_s(x,\ y) = 0, & if\ |x| \geq L \end{cases} \quad (2)$$

where h = 20 mm (R2), 40 mm (R4), or 80 mm (R8). A second vertical coordinate, z' = z − z_s (x, y), is applied to denote the height above the local surface. For validation purposes, two of the LES cases (H4 and R4) are modelled to be in accordance with the Ishihara et al. (1999, 2001) experiments.

To best reproduce the experimental results, the configuration for our numerical model is set to be the same as that in the wind tunnel experiments by Ishihara et al. (1999, 2001), except for the domain size in the spanwise direction, L_y, and the upstream necking zone. In the experiments by Ishihara et al. (1999, 2001) on a smooth 3D hill, the turbulent boundary layer (TBL) was simulated using two 60-mm-high cubic arrays placed downstream of the contraction exit, followed by 20-mm and 10-mm cubic roughness elements, covering 1.2 m of the test-section floor. The remaining 5.8 m of the test section floor was covered with plywood, which was as smooth as the hill surface. The 3D hills or 2D ridges were mounted 4.6 m downstream of the contraction exit. In the present simulation, the domain extends over (L_x, L_y, L_z) = (9, 0.65, 0.9) m^3 = (25, 1.8, 2.5) δ^3 = (90, 6.5, 9) L^3. Two nested domains (coarse and fine) are adopted, as illustrated by the red dashed lines in Fig. 1. The fine-grid domain covers the range of (L_x', L_y', L_z') = (10, 2, 3) L^3 in the x-,

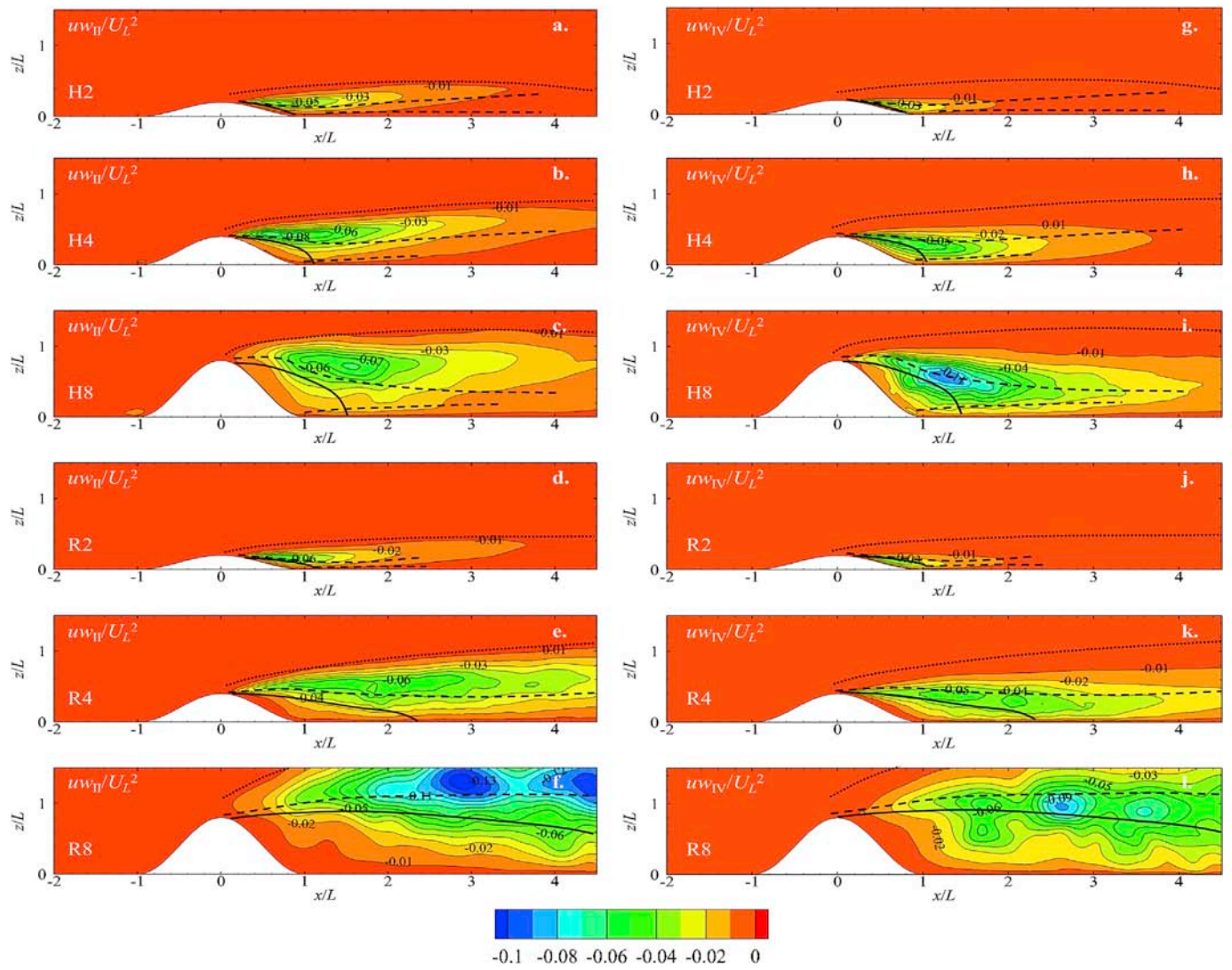

Fig. 5. Distributions of uw_{II} for (a) H2, (b) H4, (c) H8, (d) R2, (e) R4, (f) R8, and uw_{IV} for (g) H2, (h) H4, (i) H8, (j) R2, (k) R4, (l) R8, on the vertical slice of $y = 0$. The dotted lines denote the boundary of the wake depth, the dashed lines indicate the locations of peak TKE, and the solid lines show the center of the separation bubble with zero mean streamwise velocities.

y-, and z-directions, respectively. Both the upstream and the downstream fine-grid regions are $5L$ long.

The vertical grid resolutions are identical in both of the fine- and coarse-grid domains. The grid is stretched at a speed of 1.05, starting with a vertical grid spacing of 0.2 mm at the surface. A horizontal grid size of 2.0 mm is used in the fine-grid domain. Turbulence structures in the fine-grid domain are resolved with high resolution, but the resolution of the turbulence structures in the coarse-grid domain is low. Because only resolved structures are transferred from the coarse grid to the fine grid, a transition region, which allows turbulence structures to develop, must be present at the boundary of the fine-grid domain. Through the use of the correction zonal grid refinement method of Liu et al. (2016a), a buffer zone, with the horizontal grid size increased from 2.0 mm at the boundary of the fine-grid region, to 10 mm at the inner boundary of the coarse-grid region, is used. The horizontal grid shape within the buffer zone is quadrilateral, with a growth factor of 1.2. In the coarse-grid region, the horizontal grid shape is square, and a uniform grid size of 10 mm is applied. The choice of the size and resolution of our nested domains results from a compromise between constraints related to the available computational time, and the fact that the domain size should be large enough to represent the largest eddies and fine enough to represent the smallest eddies of interest.

2.2. Boundary conditions

As for the boundary conditions, a stress-free condition is used at the top of the domain ($\partial u/\partial n = 0$, $\partial v/\partial n = 0$, $w = 0$) and the spanwise sides ($\partial u/\partial n = 0$, $\partial w/\partial n = 0$, $v = 0$). Uniform wind flow with a constant speed of 5.4 m s^{-1} is set at the inlet ($u = 5.4$ m s^{-1}, $\partial p/\partial n = 0$), whereas a gradient-free boundary condition is set at the outlet boundary ($\partial u_i/\partial n = 0$, $\partial p/\partial n = 0$). Meanwhile, a no-slip condition is applied at the bottom surface ($u_i = 0$, $\partial p/\partial n = 0$).

2.3. Generated inflow

From the LES, the boundary-layer thickness in the absence of hills is nearly $\delta = 0.36m$, and the scale λ of the simulated boundary layer is about 1 : 1000, comparing the simulated boundary-layer thickness with that of the boundary-layer flow over grass plain in nature. The wind speed outside the boundary layer is measured to be $u_\infty = 5.8\,m\,s^{-1}$, where $\langle\cdot\rangle$ is a time-averaging process. As a result, the simulated boundary layer has a bulk Reynolds number $Re_b = u_\infty\delta/\nu = 1.4 \times 10^5$ and friction Reynolds number $Re_\tau = u_\tau z_0 / \nu = 0.14$, where $u_\tau = \sqrt{\tau/\rho} = 0.212$ m s^{-1}, τ denotes the time-averaged wall shear stress of the streamwise component ($\mu\partial u/\partial z$), and $z_0 = 0.01$ mm is the roughness

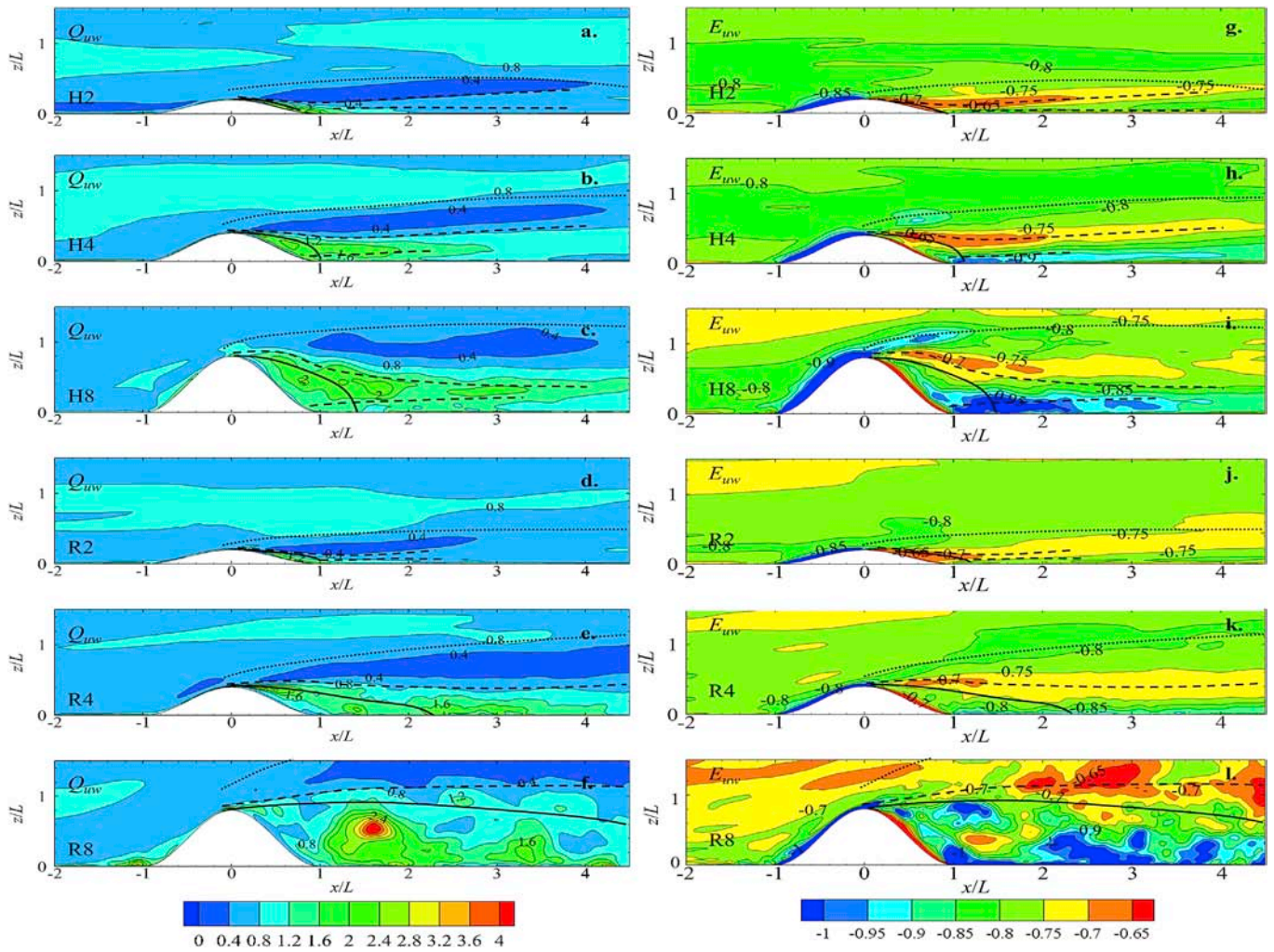

Fig. 6. Distributions of Q_{uw} for (a) H2, (b) H4, (c) H8, (d) R2, (e) R4, (f) R8, and E_{uw} for (g) H2, (h) H4, (i) H8, (j) R2, (k) R4, (l) R8, on the vertical slice of $y = 0$. The dotted lines denote the boundary of the wake depth, the dashed lines indicate the locations of peak TKE, and the solid lines show the center of the separation bubble with zero mean streamwise velocities.

height determined through a comparison of the mean streamwise velocity profile with the logarithmic law $u(z)\frac{u_\tau}{\kappa}\ln\frac{z}{z_0}$.

2.4. Case settings and space normalization

The case settings are listed in Table 1. For all of the cases, the radii are set at a constant $L = 100$ mm, and the hill heights are increased by factors of 2.0 (20 mm, 40 mm, and 80 mm) to achieve different slopes. The maximum slopes, $S_{\max}$, of H2, H4, H8, R2, R4, and R8 are 0.32, 0.63, 1.26, 0.32, 0.63, and 1.26, respectively. These settings result from the consideration that in a certain district, the higher the hill is, the steeper the hill is more likely to be, as can be seen in Fig. 2, which is a photo of a wind farm in the eastern part of China. The eastern part of China is the economic center of the country, and in this region, many wind farms are currently being built. In addition, the heights of the hills are mostly below 100 m (Li, 1987).

For the space normalization, h and L can be adopted. However, we consider that a certain wind farm will experience a certain far-field upcoming wind at a certain time, which signifies that the wind profile is independent with respect to the height of the hill. Therefore, if the space normalization is performed using h, it indicates that the far-fields wind profiles for these models are different, and the comparison will be meaningless because of the different wind conditions. In addition, if the space is normalized using h, the locations of the profiles will be, for example, $-2h$, $-1h$, $-0.5h$, $0h$, $0.5h$, $1h$, and $2h$. Therefore, for different models, the relative locations of the profiles will be different. For example, $-2h$ in H2 is located at the windward side of the hill, but $-2h$ in H8 is located far upstream of the hill, and thus comparison between them will be difficult. From the aforementioned considerations, we decided to select L instead of h to use in the normalization. We believe this selection more directly supports the real-life application of the data in the present study in the area of wind energy.

3. Results and discussions

3.1. Mean and fluctuation profiles

Fig. 3 presents the time-averaged velocities in streamwise direction, u (Fig. 3(a)), and vertical direction, w (Fig. 3(b)), and the r.m.s. of the streamwise fluctuation, σ_u (Fig. 3(c)), spanwise fluctuation, σ_v (Fig. 3(d)), and vertical fluctuation, σ_w (Fig. 3(e)), on the $y = 0$ slice, superimposed on which are the experimental data for H4 and R4 by Ishihara et al. (1999, 2001).

At $x = -4L$, $-3L$, and $-2L$, the profiles of mean velocities and fluctuations appear to be almost identical for all the cases. At the windward foothill, where $x = -1L$, u decelerates because of the blockage effects exerted by the hills, which is substantially more evident when the hills are steeper or when the shape is a 2D ridge. An acceleration of w, which

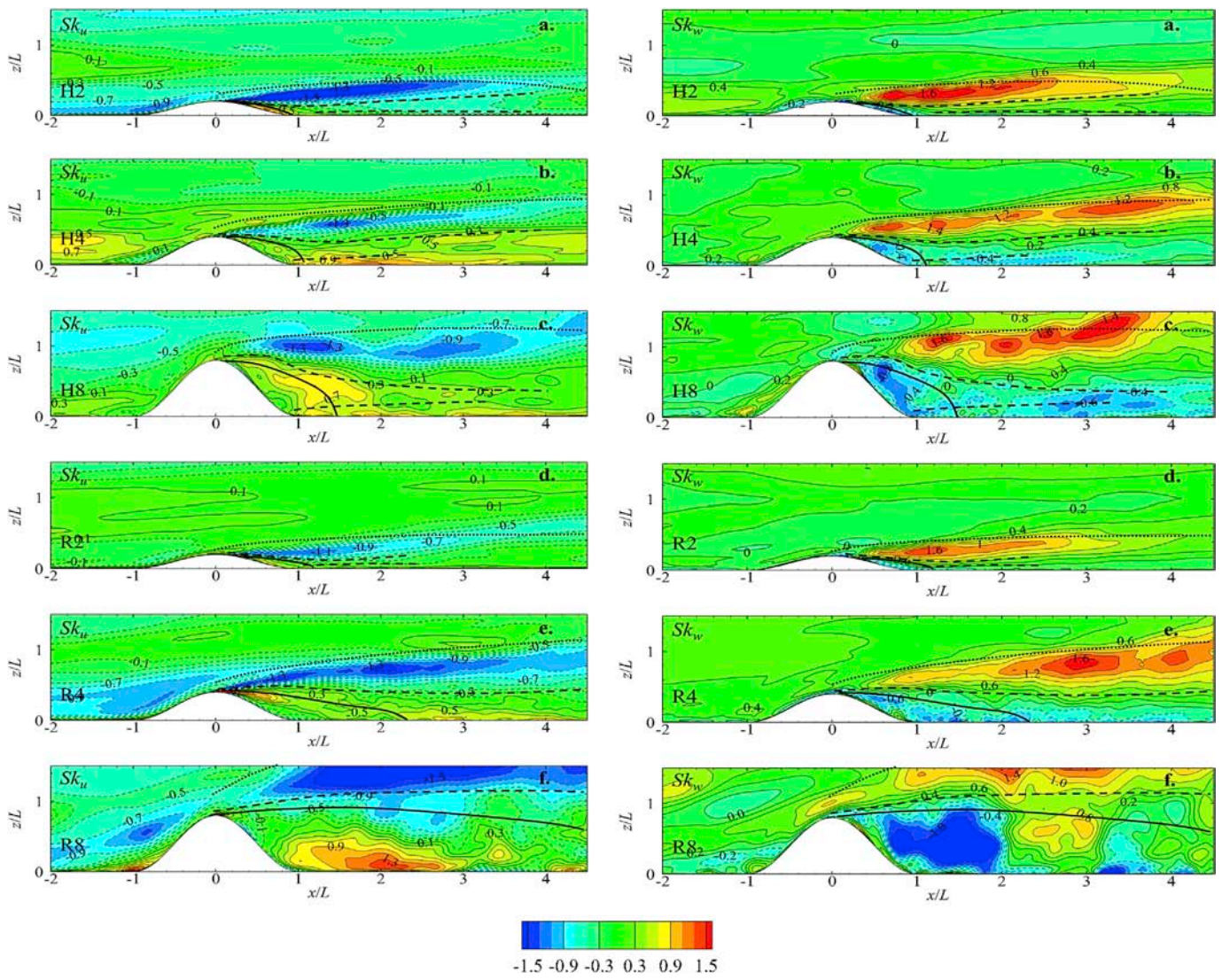

Fig. 7. Distributions of Sk_u for (a) H2, (b) H4, (c) H8, (d) R2, (e) R4, (f) R8, and Sk_w for (g) H2, (h) H4, (i) H8, (j) R2, (k) R4, (l) R8, on the vertical slice of $y = 0$. The dotted lines denote the boundary of the wake depth, the dashed lines indicate the locations of peak TKE, and the solid lines show the center of the separation bubble with zero mean streamwise velocities.

results from the slope of the hill, is also observed here, and this acceleration increases as the hill slopes increase. Furthermore, still at $x = -1L$, sharp increases in the σ_u profiles at the near-wall regions can be clearly identified in H8 and R8.

On the way up to the crest, the deceleration of u and acceleration of w are maintained, whereas a notable speedup of u appears at $x = 0L$ in all cases. As for σ_u and σ_w, an increase in σ_u and a reduction in σ_w over the hilltop are observed. In accordance with the rapid distortion theory proposed by Hunt and Carruthers (1990), the increase in σ_u and the reduction in σ_w over the hilltop ought to be caused by the eddies of the upwind flow being stretched by the mean flow at the hilltop, resulting in elongated eddies in the streamwise direction but flattened eddies in the vertical direction. Hill crest is the location where the wind usually shows largest speed up, and as the major velocity component, u should be paid much attention. In Appendix 2, an analytical model for predicting the profiles of u at the hill crest is proposed.

As the flow further moves downstream to the near-wake region $x = 0.5L$, the presence of the recirculation bubble causes the flow to be more complex. For u, distinct from those upstream the summit, an inflection point on the profile could be easily identified, at which the vertical gradient of u exhibits its maximum value, suggesting massive wind shear and turbulence productions. Nevertheless, the maximum vertical gradient of u is surprisingly almost unchanged, regardless of the steepness and shape of the topographies. Furthermore, the effects of the topography on the w profiles can stretch to the remote wake regions in H8, R4, and R8. Despite this, the distortions of the w profiles vanish very quickly just downstream the reattachment points in H2, H4, and R2. Interestingly, the fluctuations σ_u and σ_v at $x = 0.5L$ peak at an elevation of about h, and the magnitudes of the peaks appear to be independent of the hill slope and hill shape. However, σ_w is weakened as the shape is changed from 3D hill to 2D ridge when $h = 80$ mm.

In the far wake region $x \geq 1L$, the recovery of the mean velocities is found to be very difficult as the hill slope is increased or the shape is changed from 3D hill to 2D ridge, indicating the stronger blocking effect of the 2D ridges. In the very far wake region, $x \geq 3L$, the wind speed reduction remains evident, and there is no similarity with the corresponding 3D hill case H8. Concerning the fluctuations, the σ_u profiles are characterized by the peaks being located at the inflection points on the u profiles in all cases. However, an additional peak on the σ_u profile located near the ground is identified in H8, which is not observed in R8.

It is important that the mean velocities and the fluctuations for H2 and R2 are almost the same, indicating that when the hill slope is below 0.32, the hill shape effect can be neglected. As the hill slope increases, the differences between 3D hill and 2D ridge become stronger, and the

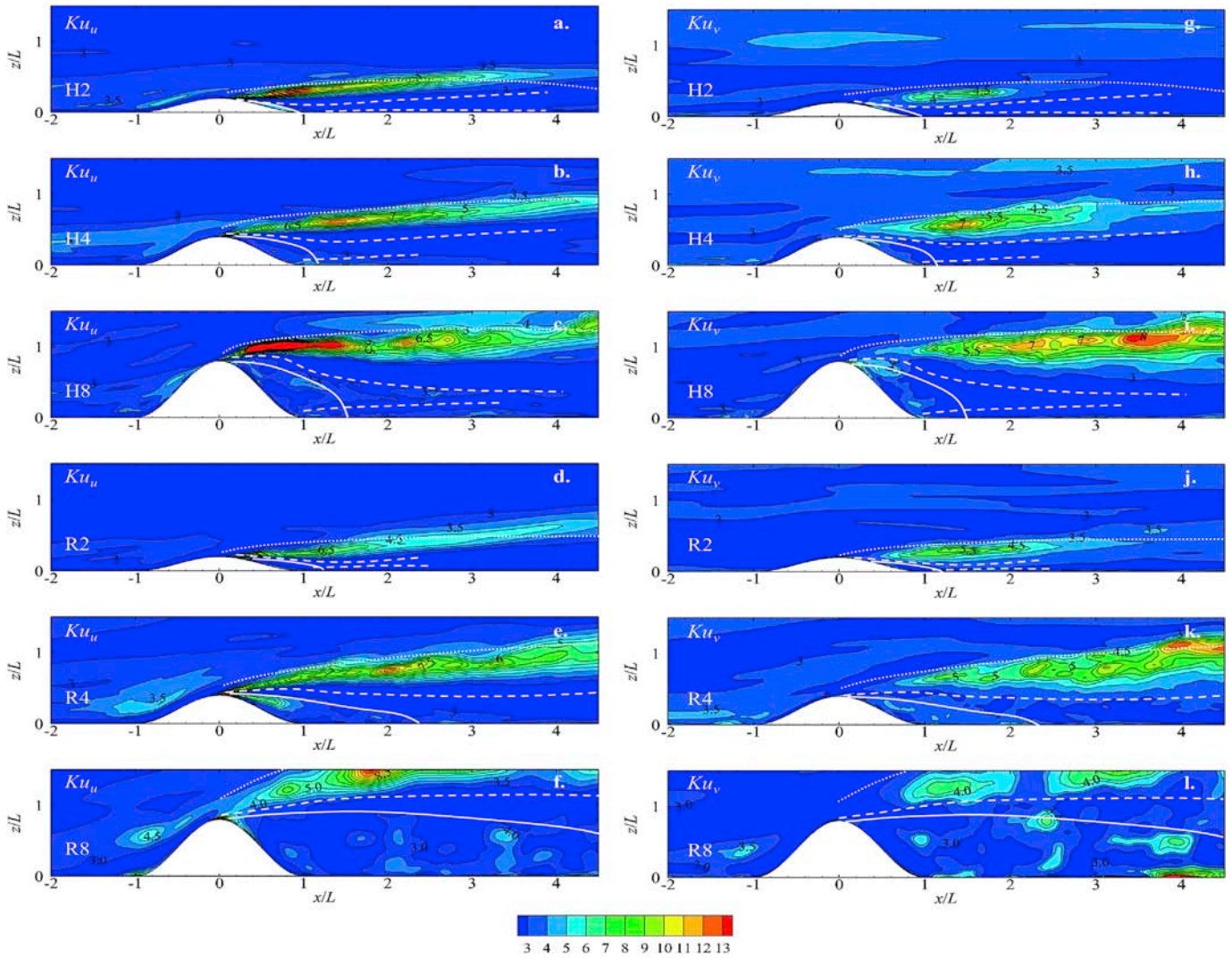

Fig. 8. Distributions of Ku_u for (a) H2, (b) H4, (c) H8, (d) R2, (e) R4, (f) R8, and Ku_v for (g) H2, (h) H4, (i) H8, (j) R2, (k) R4, (l) R8, on the vertical slice of $y = 0$. The dotted lines denote the boundary of the wake depth, the dashed lines indicate the locations of peak TKE, and the solid lines show the center of the separation bubble with zero mean streamwise velocities.

similarities between 3D hill and 2D ridge almost disappear for H8 and R8. The reason should be that the lateral flow entering the recirculation bubble of a 3D hill becomes weak as the hill slope decreases. Moreover, for the 2D ridge, there is no such lateral flow. As a result, the flow fields of the 3D hills and 2D ridges will become similar as the slope decreases.

3.2. TKE and turbulence flux

TKE, $k = 1/2u'u' + v'v' + w'w'$, is illustrated in Fig. 4(a–f). Obviously, for all the cases, TKE concentrates at the upper part of the recirculation bubble. In addition, the magnitude of TKE becomes stronger when the hill gets steeper, indicating a much more energetic interaction between the separated bubble and the shear layer. We can also find that there are two peak regions on the TKE plots for 3D hills, no matter how steep the hills are. However, this phenomenon is not observed in the cases of 2D ridges when S_{max} is larger than 0.64, which should be due to the different turbulence structures between them, as will be depicted in Appendix-1. In addition, the TKE is strengthened as the hill shape changes from 3D hill to 2D ridge, because of the stronger mixing effect from the 2D ridges.

The vertical turbulent flux $u'w'$ is illustrated in Fig. 4(g–l). A rapid decay of $u'w'$ as the flow enters the recirculation bubble can be clearly identified for all the cases. $u'w'$ reaches its maximum at the locations close to the upper boundary of the bubble. This feature can possibly be accounted for by the strong streamwise acceleration of the flow as it moves upward from the bubble to the ejection region. In addition, the vertical turbulent flux is found to be increased as the hill slope increases or as the shape of topography changes from 3D hill to 2D ridge. Moreover, the increase in the vertical turbulent flux due to the change in topography from 3D hill to 2D ridge is found to be strengthened as the slope increases.

The vertical turbulent flux in the second quadrant, $uw_{II} = u'w'$ for the events ($u' < 0,\ w' > 0$) caused by ejection, and the vertical turbulent flux in the fourth quadrant, $uw_{IV} = u'w'$ for the events ($u' > 0,\ w' < 0$) caused by the sweep motion, are further examined (see Fig. 5). Large uw_{II} appears in the shear layer region, whereas large uw_{IV} appears below the shear layer. In general, both the ejection motion and sweep motion are enhanced as the topography becomes steeper. For the 3D hills, the sweep motion is found to be stronger than the ejection, whereas the reverse is true for the 2D ridges. In addition, the ejection and sweep motions of the fluids are more energetic if the shape is changed from 3D hill to 2D ridge, which may be because the vortex in the lateral direction is more difficult to be broken for the 2D ridges.

To show the relative importance of the sweeps or ejections to the vertical turbulent flux, $Q_{uw} = uw_{IV}/uw_{II}$ is plotted in Fig. 6(a–f). The contour line of $Q_{uw} = 1.0$, i.e., $uw_{II} = uw_{IV}$, almost coincides with the locations of peak TKE, and the largest Q_{uw} appears in the locations just

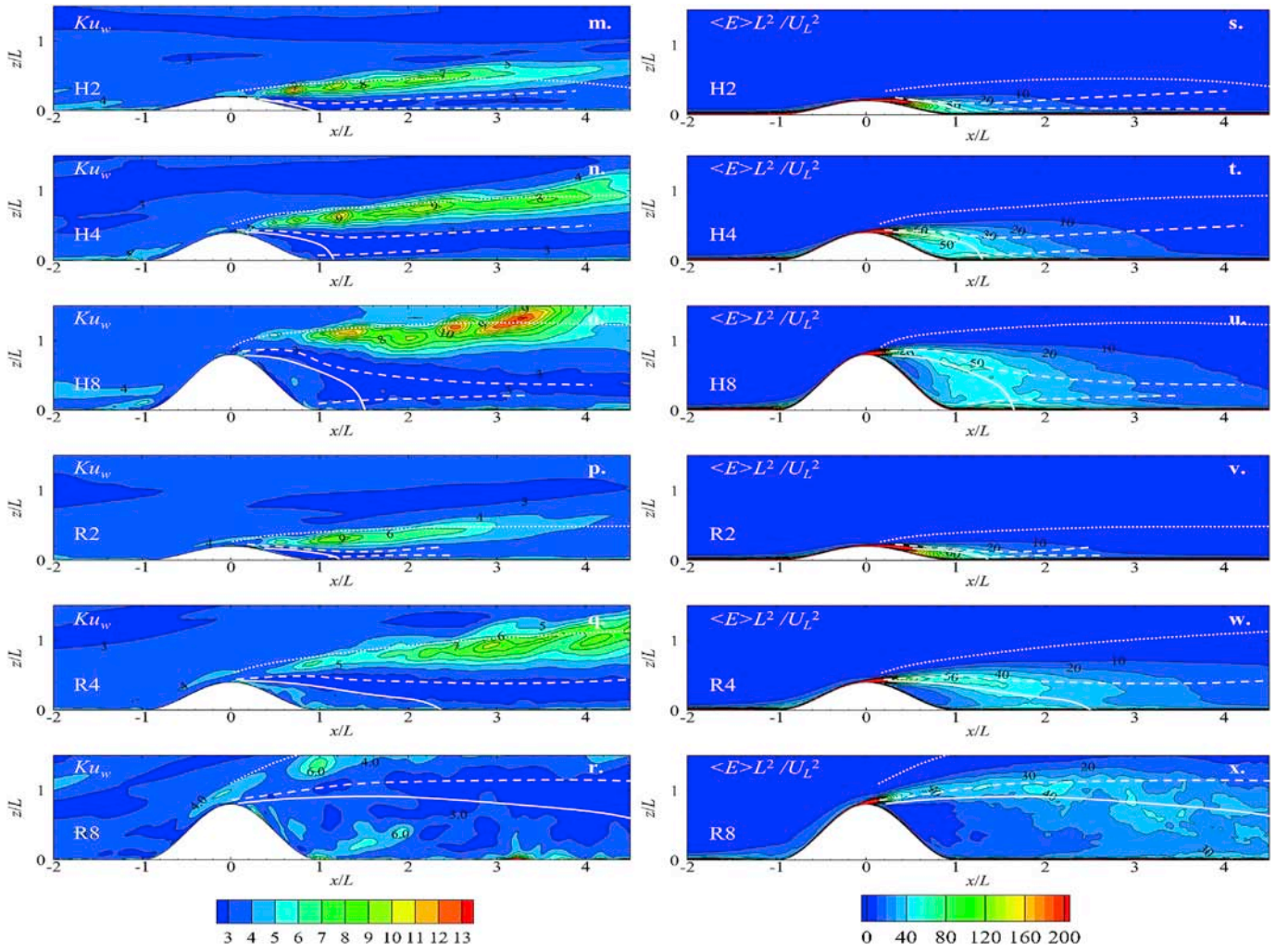

Fig. 9. Distributions of Ku_w for (a) H2, (b) H4, (c) H8, (d) R2, (e) R4, (f) R8, and E for (g) H2, (h) H4, (i) H8, (j) R2, (k) R4, (l) R8, on the vertical slice of $y = 0$. The dotted lines denote the boundary of the wake depth, the dashed lines indicate the locations of peak TKE, and the solid lines show the center of the separation bubble with zero mean streamwise velocities.

downstream of the recirculation for the 3D hills, and roughly in the recirculation bubble for the 2D ridges. Q_{uw} also exhibits evident increase as the slope of the topography increases or the shape changes from 3D hill to 2D ridge, indicating the more energetic sweep motions of the flows for the steeper hills and 2D ridges, which should be due to the stronger negative pressure caused by their respective topographies.

The exuberance, $E_{uw} = (uw_{\mathrm{I}} + uw_{\mathrm{III}})/(uw_{\mathrm{II}} + uw_{\mathrm{IV}})$, where $uw_{\mathrm{I}} = u'w'$ for the events ($u' > 0$, $w' > 0$), and $uw_{\mathrm{III}} = u'w'$ for the events ($u' < 0$, $w' < 0$), is plotted in Fig. 6(g–l). E_{uw} is a measure for the relative effectiveness of the momentum exchange (through ejections and sweeps) compared to the interaction quadrants. In this way, we can more easily assess how organized/disorganized the turbulence becomes and how the hill shape affects this turbulence. At the location just above the recirculation bubble, E_{uw} evidently exhibits its maximum values for all of the cases, indicating the strongest organized motions at this location. E_{uw} is close to 1 near the ground just downstream of the recirculation bubble, which signifies that the momentum exchange (through ejections and sweeps) is almost equal to the interaction quadrants, or that the turbulence is fully mixed and reveals homogeneous properties. As the slope increases, the region with $E_{uw} \approx 1$ covers a larger area, and if the shape is changed to a 2D ridge, the area of $E_{uw} \approx 1$ is shrunk, which indicates that, for the 2D ridges, the organized turbulence can extend to a region much closer to the ground.

3.3. Skewness and kurtosis

The skewness of u_i, $Sk_{u_i} = u_i'^3/u_i'^{3/2}$, provides information about the symmetry of the probability density function (PDF) of u_i. Notably, the skewness of any univariate normal distribution is 0. The large negative Sk_u is primarily confined within the shear layer region ($Sk_u < -1.0$), as shown in Fig. 7(a–f). Not only does this indicate an asymmetric distribution of streamwise velocity around its averaged value (the velocity with largest probability is larger than the mean value), it also demonstrates a high likelihood of strong intermittent upwind gust events. The negative Sk_u in the shear layer recovers to the ambient turbulence level ($Sk_u = -0.3$) as the flow moves downstream. Meanwhile, when the hill is steeper, this recovering process appears to be substantially quicker, which is attributed to the stronger mixing effects of the higher hill. Sk_w and Sk_u exhibit similar distributions but opposite signs, as illustrated Fig. 7(g–l). The positive Sk_w just downstream the top of the topographies indicates the presence of strong intermittent upward motions, as has also been observed from the $u'w'$ plots in Fig. 4(g–l). Furthermore, the concentration of the positive Sk_w appears further downstream after the shape is changed from 3D hill to 2D ridge.

The kurtosis $Ku_{u_i} = u_i'^4/u_i'^2$ provides information on the flatness of the velocity PDF. Noticeably, the kurtosis of three velocity components [Ku_u

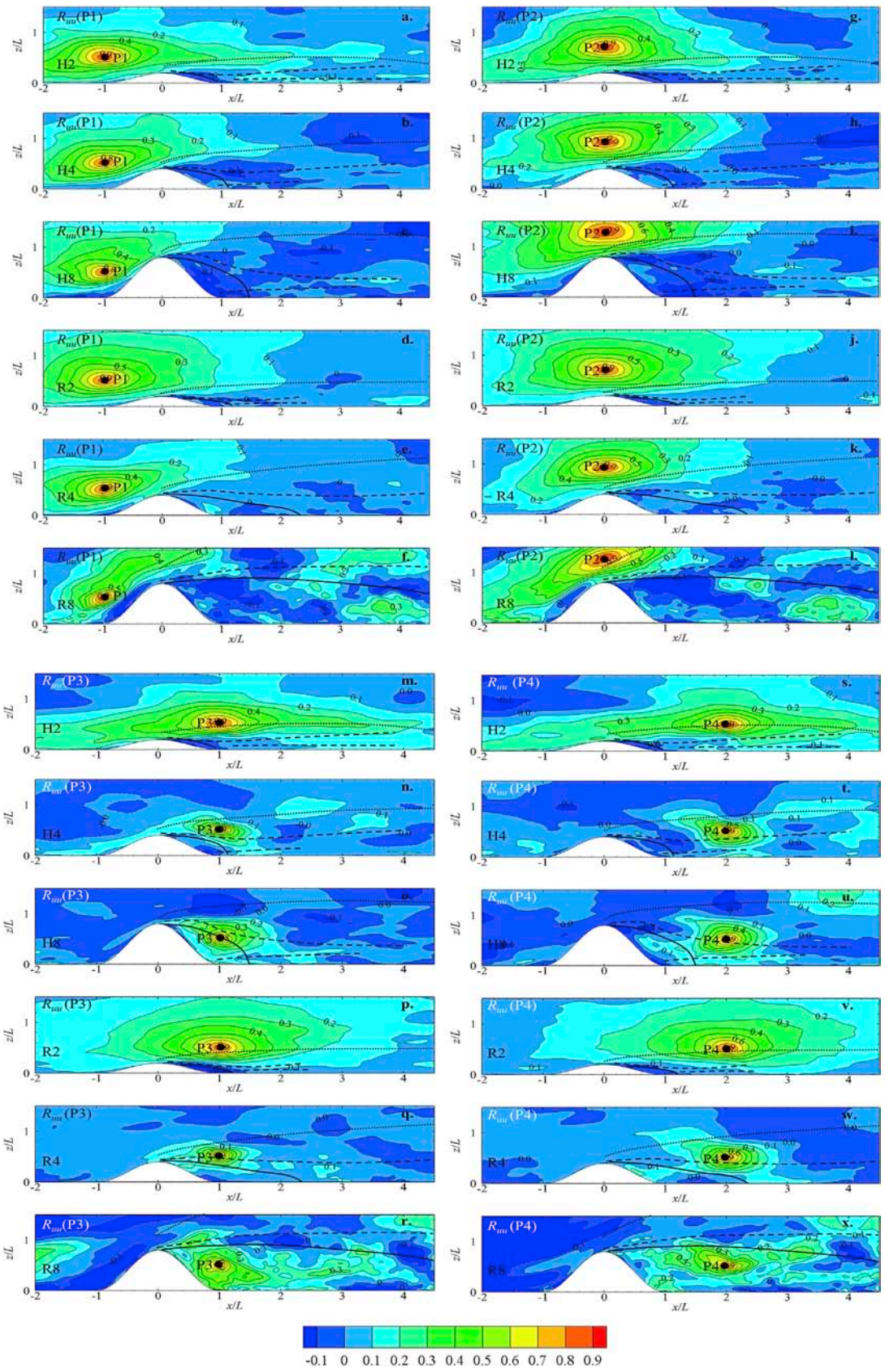

Fig. 10. Contours of R_{uu} for P1 in (a) H2, (b) H4, (c) H8, (d) R2, (e) R4, (f) R8, and for P2 in (g) H2, (h) H4, (i) H8, (j) R2, (k) R4, (l) R8, and for P3 in (m) H2, (n) H4, (o) H8, (p) R2, (q) R4, (r) R8, and for P4 in (s) H2, (t) H4, (u) H8, (v) R2, (w) R4, (x) R8, on the vertical slice of $y = 0$. The dotted lines denote the boundary of the wake depth, the dashed lines indicate the locations of peak TKE, and the solid lines show the center of the separation bubble with zero mean streamwise velocities.

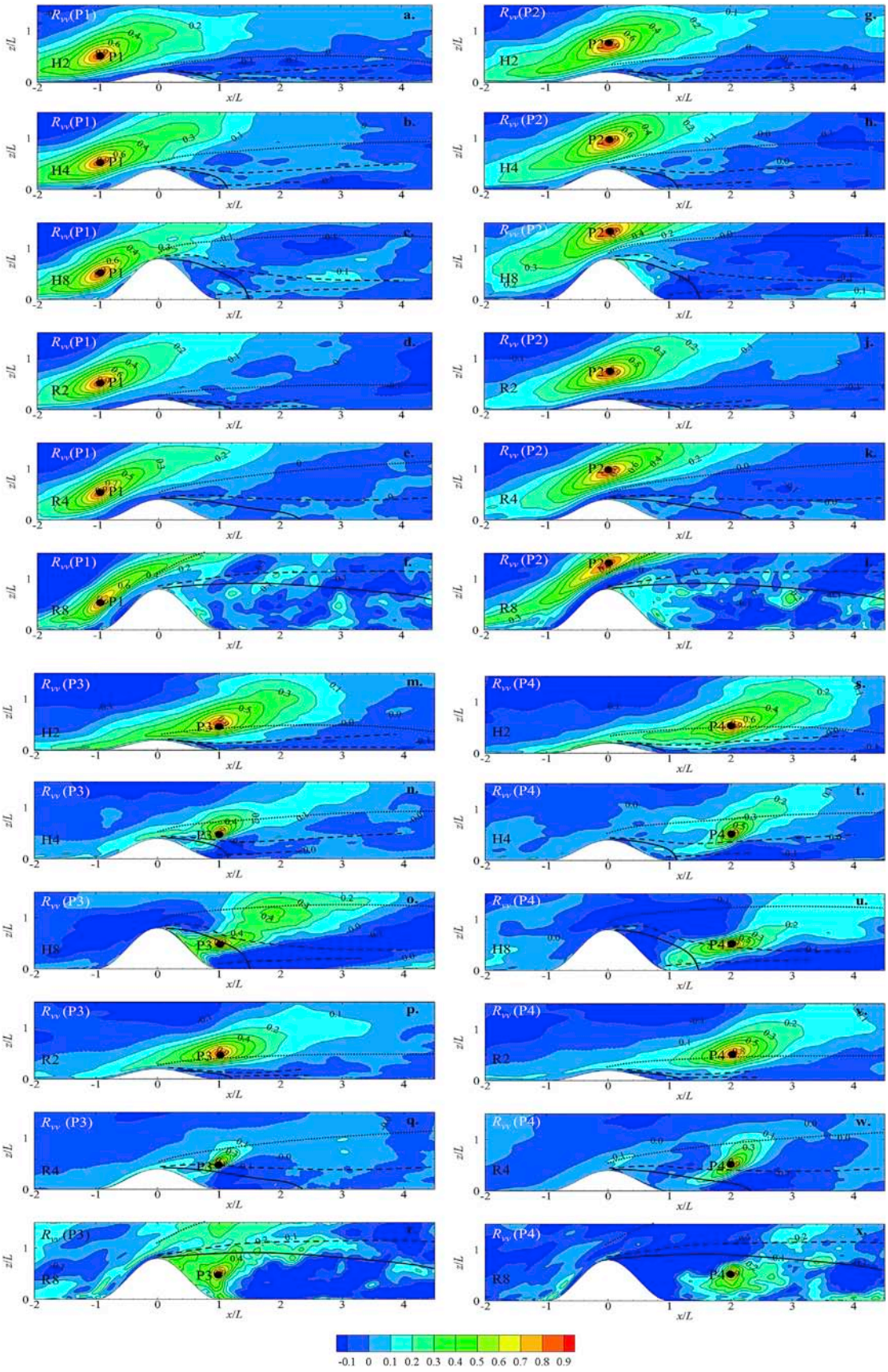

Fig. 11. Same as Fig. 10 but for R_{vv}.

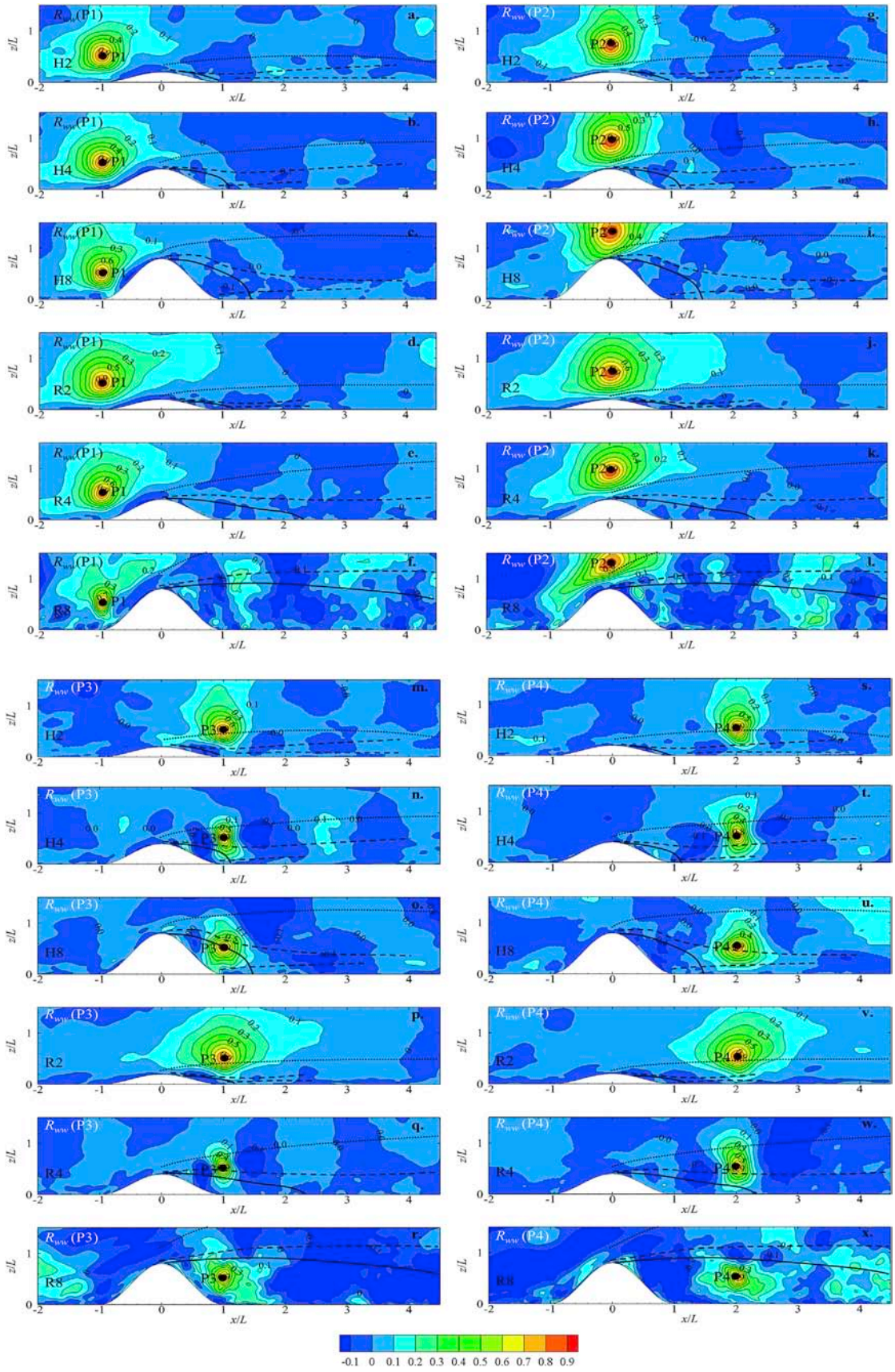

Fig. 12. Same as Fig. 10 but for R_{ww}.

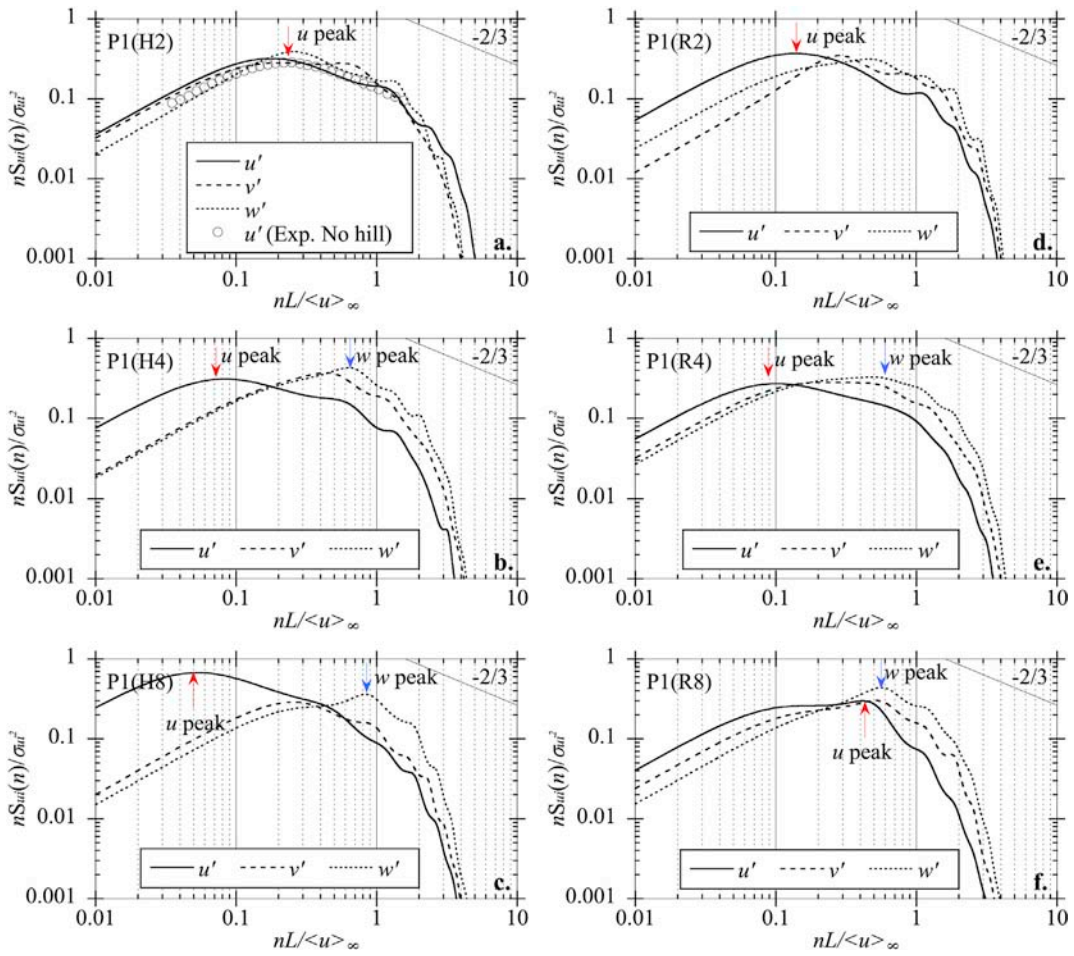

Fig. 13. Pre-multiplied spectra of three velocity components, nS_u, nS_v, and nS_w, at the monitoring point, P1, for (a) H2, (b) H4, (c) H8, (d) R2, (e) R4, and (f) R8.

(Fig. 8 a–f), Ku_v (Fig. 8 g–l), and Ku_w (Fig. 9 a–f)] exhibit similar distributions with broadly identical magnitudes in each case. The peak Ku_{ui} is just at the upper boundary of the wake, indicating a very steep shape of the velocity PDF. Ku_{ui} approaches the value of 3 close to the ground, implying either normal distribution or a fully mixed flow. Moreover, the thicknesses of the regions with large kurtosis appear to vary slightly for the hills or ridges with moderate and large slopes (H4 and H8), and based on a comparison with the distribution of Ku_{ui} of 3D hills and 2D ridges, the regions with large kurtosis clearly are thicker for the 2D ridges.

Enstrophy $E = 1/2\omega_i\omega_i$ is involved in the quantification of the local rotation rate, as shown in Fig. 9(g–l). E is clearly seen to intensify at the summit. Downstream the summit, Epeaks at nearly the same positions of peak TKE, suggesting that turbulent structures in the wakes are largely characterized by local rotations other than the strain of the flow. When the hill turns steeper, E in the wake basically remains unchanged. Close to the center of the recirculation bubble, the rotations nearly disappear for H8, R4, and R8. Moreover, the regions with weak rotation are increased as the topography changes from 3D hill to 2D ridge.

3.4. Two-point correlations

Spatial information associated with the size of the major turbulent structure is provided by two-point correlations between velocity components (R_{uu}, R_{vv}, R_{ww}), as illustrated in Figs. 10–12. $R_{u_iu_i}(x, y, z) = u_i'(x, y, z)u_i'(x_{ref}, y_{ref}, z_{ref})/[\sigma_{u_i}(x, y, z) \cdot \sigma_{u_i}(x_{ref}, y_{ref}, z_{ref})]$ and (x_{ref}, y_{ref}, z_{ref}) are the coordinates of the reference points (P1, P2, P3, and P4). z' for P1, P2, P3, and P4 is a constant equal to 50 m in full scale, which is 5 cm (0.5L) in the present simulation. The selection of the reference points is performed based on the considerations that the hub-height is nearly a constant 50 m for the commonly used 1.0 MW wind turbines in China, and that the height of the wind turbines is independent with respect to the height of the hill.

For the streamwise component, at P1 (Fig. 10 a–f), on the way up to the summit, the correlated contours of R_{uu} are found to be more inclined toward the upwind side, and the downstream part of streamwise correlation is found to extend further than the upstream part. In the recirculation bubble, an area with negative sign just beneath the center of the bubble is easily observed because of the presence of the backward flow. In H8, the correlated area of R_{uu} shrinks and becomes far shorter than those in H2 and H4 because of significant blockage effects from the topography. The correlated contour of R_{uu} becomes more inclined and the correlated area is shrunk further as the shape of topography changes from 3D hill to 2D ridge. At P2 (Fig. 10 g–l), the streamwise correlation is enhanced with the increase in h. A nearly elliptical area with large elongation in the streamwise direction is identified at P2, which reveals the contributions of large-scale turbulent eddies in TBL. In addition, the non-correlation between the wind at P2 and that in the wake indicates different turbulence structures both over and beneath the shear layer. For H2 and R2, the correlated areas of R_{uu} at P3 (Fig. 10 m–r) and P4 (Fig. 10 s–x) vary at a slow pace as compared to that at P2. However, R_{uu} is weakened considerably in H4, H8, R4, and R8 because of the highly mixing effects and the substantially small sizes of turbulence in the shear layers. As the reference point moves downstream from P3 to P4, the correlated areas are expanded because of the recovery process of the wake turbulence to ambient turbulence.

For the spanwise component, R_{vv} (Fig. 11) is similar to R_{uu}, except for the more inclined shape of the former. In addition, in H4, H8, R4, and R8, the spanwise correlations at P3 and P4 are characterized by large positive

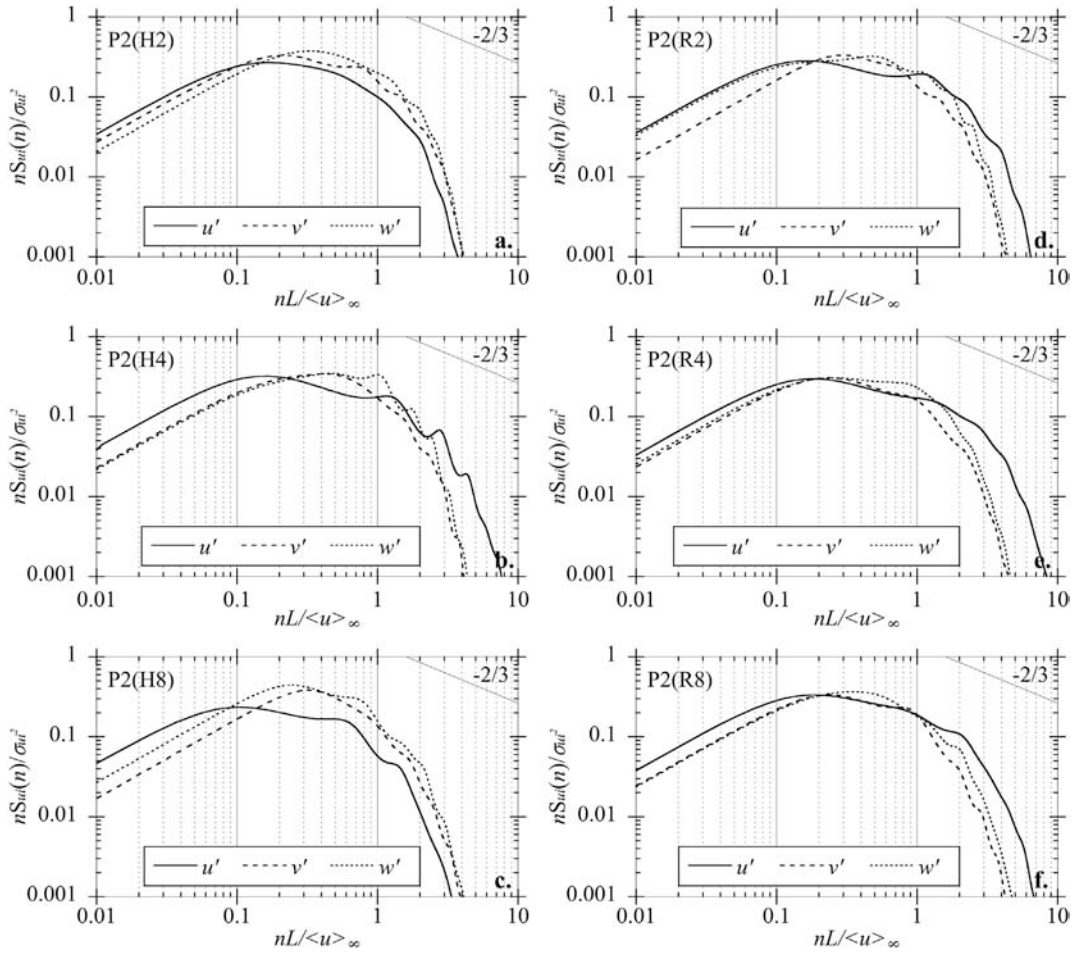

Fig. 14. Same as Fig. 13 but for P2.

values aloft and large negative values close to the ground. The magnitude and extension of R_{vv} decreases from H2 to H4 and then increases again from H4 to H8, which is also found in the corresponding 2D ridges. This should be the result of the different relative locations of the reference points over the topographies with different heights. For H2 and R2, P3 and P4 are above the shear layer regions where the flow structures are controlled mainly by the ambient turbulent flows; for H4 and R4, P3 and P4 are in the shear layer regions where the mixing effects are strong; and for H8 and R8, P3 and P4 are in the regions with more organized flow structures.

For the vertical component, R_{ww} (Fig. 12), compared with R_{uu} and R_{vv}, at P1 and P2 is roughly circular with a slight elongated size in the vertical direction. At P3 (Fig. 12 m–r) and P4 (Fig. 12 s–x), periodic behavior (the sign changes from + to –) on the distribution of R_{ww} is apparent for H2, H4, and H8, with wavelengths of about 1.0L, 1.2L and 1.6L, respectively. This periodic behavior is also found in the 2D ridges, and the wavelengths are almost same as those of the corresponding 3D hills. In addition, the periodic behavior becomes more evident when the reference point is located in the shear layer region (H4).

3.5. Spectra

Spectral analysis provides information about how energetic the turbulence structures are and how the energy is distributed among the eddy scales present in the flow, to shed light on the dynamics of the eddy motions. The spectral (S_u, S_v, S_w) is pre-multiplied by the frequency n and further normalized by u'^2, v'^2, and w'^2, respectively, as shown in Figs. 13–16. For the horizontal axis, the frequency n is normalized by u_∞/L to clarify the relative sizes of the eddies to those of the same hills studied by Ishihara et al. (1999). The time signals of the flow at P1–P4 are recorded over a period of 400 L/u_∞, and the maximum-entropy method (MEM) is adopted to provide smoothed spectra. A more detailed introduction about this method can be found in the studies by Kay and Marple (1981) and Press et al. (2007).

At P1, the spectrum displays a −2/3 slope in the inertial subrange for H2, which conforms to Kolmogorov's hypothesis (Kolmogorov, 1941). However, there is a steep decline beyond this inertial range ($nL/u_\infty > 1.5$), which fails to be observed in the experiments by Ishihara et al. (1999) and Cao and Tamura (2006). This discrepancy suggests that the present simulations are incapable of resolving small-scale eddies in a broad dissipation range because of the filtering effects (the filter width Δ is 2 mm in the present LES) from the SGS model, which is also observed in the study by GarcÍA-Villalba et al. (2009). Nevertheless, motions with relatively low frequencies are resolved accurately, as seen in Fig. 13(a), where data for the streamwise component from the experiment by Ishihara et al. (1999), without the topography, are also plotted, and good agreements are achieved, indicating that the flow at P1 is seldom affected by the topography because of the relatively high elevation of the reference point as compared with the height of the hill (H2). As the slopes of the 3D hills increase, there are an evident shift of the peak frequency of the streamwise velocity to the low-frequency range, and an evident shift of the peak frequency of the vertical velocity to the high-frequency range. For H8, the peak frequencies of the streamwise and vertical velocities occur at about 0.05 u_∞/L and 0.8 u_∞/L, respectively, which are almost the same as the frequencies of the wandering motion of the major core and the occurrence of the circular tubes observed from the previous instantaneous flow-fields visualization. This observation should imply

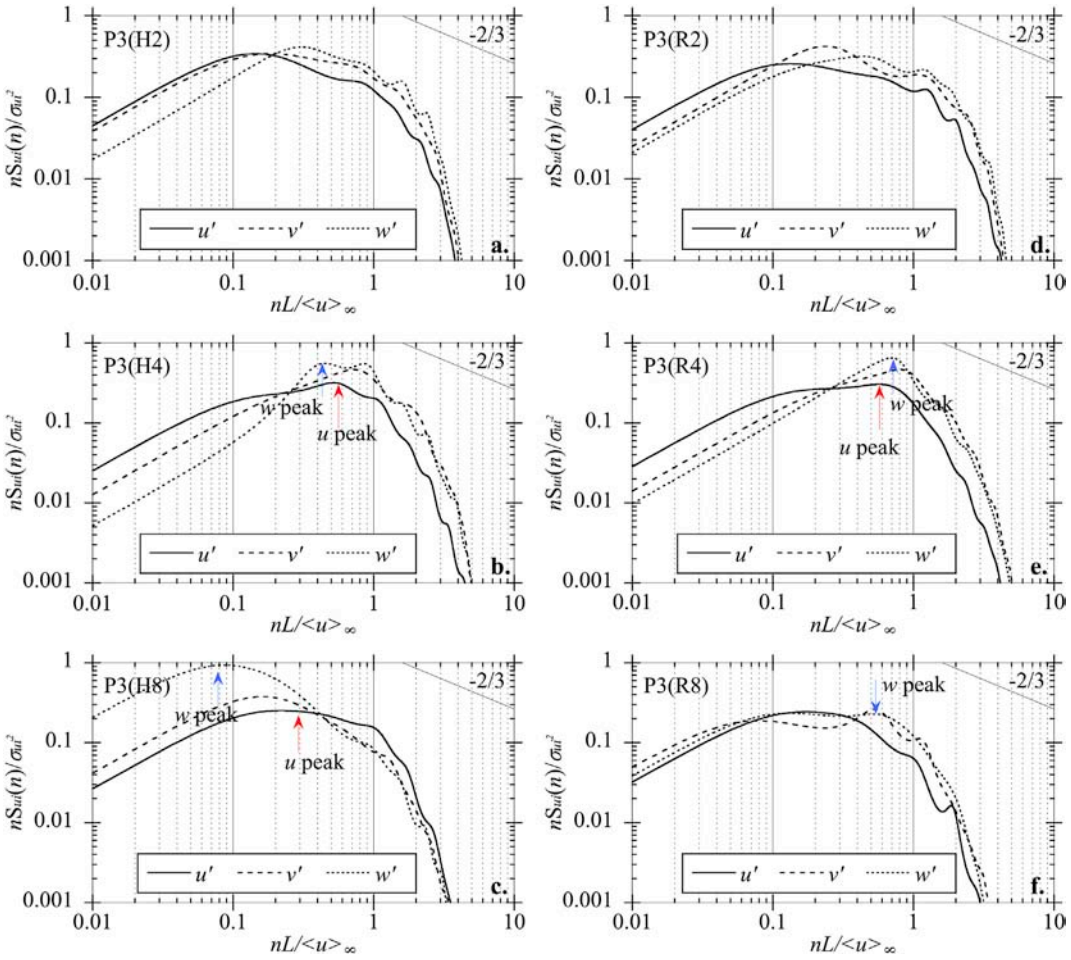

Fig. 15. Same as Fig. 13 but for P3.

that the organized flow structure downstream the topography can even affect the flow fields upstream of the topography. For the 2D ridges, the increases in the slopes will make the energy of the streamwise and vertical velocities concentrated in the higher-frequency range. For R8, the concentrated energy of the streamwise and vertical velocities occurs at a frequency of about $0.6\,u_\infty/L$, close to the frequency of the periodical shedding of the spanwise vortex observed in Fig. 13(f).

At P2, which is safely higher than the shear layer region, the properties of the turbulent flow fields should be controlled mainly by the ambient turbulence. Therefore, the shapes of the spectrum are similar to those without the topography (Fig. 14).

At P3, the spectra of H2 and R2 are still similar to those without the topography, because the reference point is about 2 times as high as the shear layer. Interestingly, H4 and R4 exhibit similar distributions of the spectrum at P3, peaking at a frequency of around $0.7\,u_\infty/L$, because of the close frequency of the generation of the circular tubes in the wake of H4 and the frequency of the hairpin structure in R4, as observed in Fig. A-4 (c, f). In H8, the roles played by the streamwise velocity and the vertical component seem to be changed at P3 (Fig. 15 f) in comparison with those at P1 (Fig. 13 f). This change is considered to be associated with the change in the flow directions. The flow with upward motion at P1 will change its direction to streamwise after it passes the hill top because of the extension of the recirculation bubble, and the flow with horizontal motion at P1 will change its direction to upward after it enters the recirculation bubble because of the bubble negative pressure. For R8, the high-frequency motion of the spanwise vortex, which appears at about $0.6\,u_\infty/L$, is identified.

At P4, the effects from the topographies become weak, and the shape of the spectrum returns to be similar to that in the ambient turbulence, as shown in Fig. 16, where the experimental data by Ishihara et al. (1999) are also plotted in Fig. 16(b), showing good comparison with the present LES.

4. Conclusions

LES is applied to conduct investigation into the effects of the hill slopes on the flow fields over 3D hills. Three hills with varying slopes are numerically examined. The mean velocities, r.m.s. of the fluctuating velocities, TKE, vertical momentum flux, two-point correlation, spectra, and visualized flow structures are systematically studied. The findings in the present LES are summarized as follows.

i. A small secondary recirculation in the very near wake region ($0 < x < 0.35L$) is identified. This counterclockwise rotating structure exists irrespective of the steepness of the topography. The length and position of this rotating structure do not vary significantly as the slope increases. However, after the shape is changed from 3D hill to 2D ridge, the secondary recirculation becomes thinner.
ii. The mean velocities and the fluctuations for H2 and R2 are almost the same. As hill slope increases, the difference between the 3D hill and the 2D ridge becomes stronger, and the similarities between the 3D hill and 2D ridge almost disappear for H8 and R8. The maximum vertical gradient of mean streamwise velocity in the near wake is almost the same no matter how steep the topography is and what the shape of the topography is. The velocity fluctuations at $x = 0.5L$ peak at an elevation of about h, and

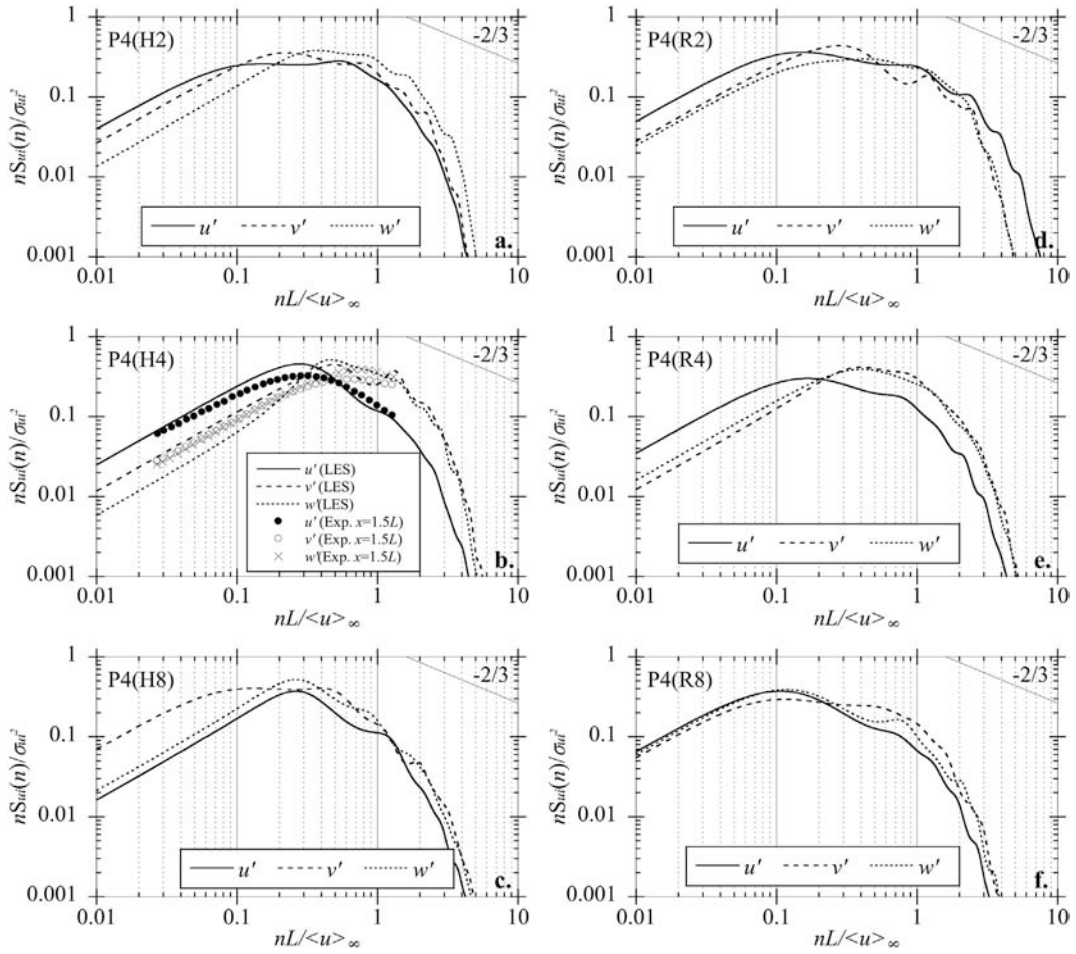

Fig. 16. Same as Fig. 13 but for P4.

the magnitudes of the peaks appear to be independent of the slope and the shape.

iii. Concerning the streamwise velocity, the energy of the streamwise velocity is concentrated in the low-frequency range at P1 of H4 and H8, and the frequency is reduced substantially from 0.08 u_∞/L to 0.05u u_∞/L as the slope increases from H4 to H8. The energy of the flow is concentrated at the high-frequency range at around 0.7 u_∞/L for the cases of R4 and R8, because of the periodic generation of the hairpin structure in R4 and the periodic shedding of the spanwise vortex in R8.

iv. A sort of spiral structure can be identified through a visualization of the turbulence structures of the flows over the 3D hills, and the pitch of the spiral appears to be narrowed as the hill slopes increase. Moreover, this spiral structure disintegrates into separated circular tubes for H8. For the ridges, the wandering of the major core is found for R2, and a hairpin structure is identified for R4, whereas the hairpin structure disappears and a vortex with a long spanwise size occurs periodically for R8.

Declaration of competing interest

The authors declare that they have no known competing financial interests or personal relationships that could have appeared to influence the work reported in this paper.

CRediT authorship contribution statement

Zhenqing Liu: Conceptualization, Methodology, Investigation, Resources, Writing - original draft, Writing - review & editing, Project administration, Visualization, Supervision, Project administration, Funding acquisition, Formal analysis, Data curation. **Wei Wang:** Investigation, Visualization. **Yize Wang:** Writing - review & editing, Visualization. **Takeshi Ishihara:** Writing - review & editing.

Acknowledgements

This study is funded by the National Natural Science Foundation of China (51978307).

Appendix-1 General characteristics of the flow fields

Fig. A-1 shows a snapshot of two iso-surfaces of spanwise vorticity $\omega_y = \partial w/\partial x - \partial u/\partial z = -15\ s^{-1}$ and $15\ s^{-1}$ of the TBL in absence of the topographies. Once the flow passes the roughness-block region, strong turbulent flow fields are generated. Further downstream, the flow is shown to experience a noticeable boundary-layer growth. Just after the outlet of the fine-grid domain, the turbulence almost vanishes because of the linear stretching of the streamwise grid.

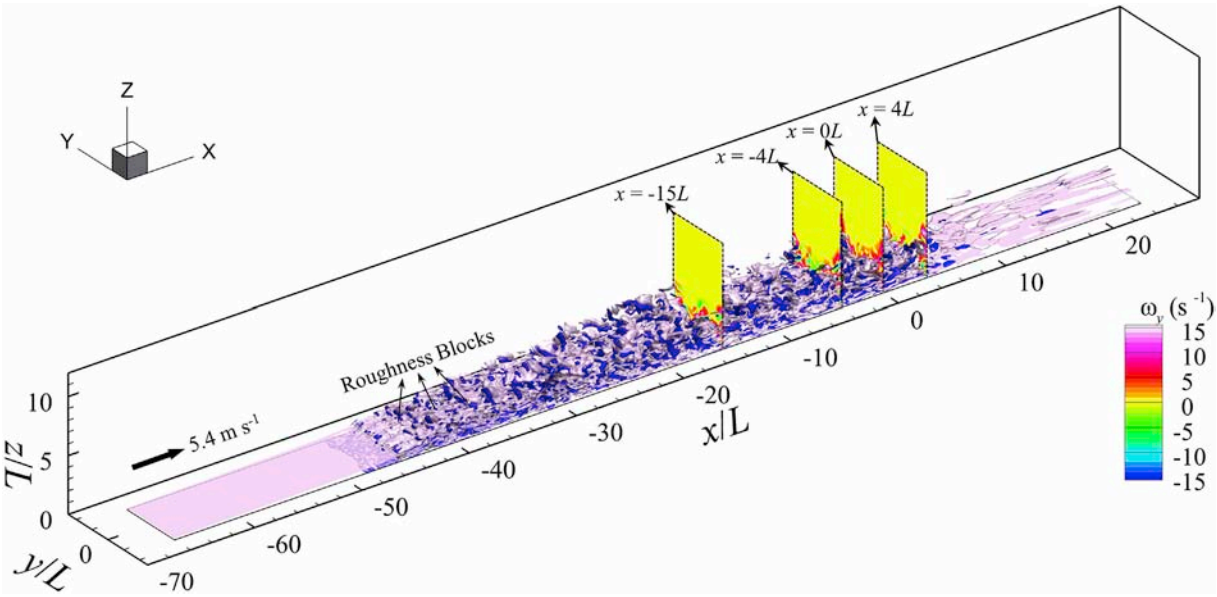

Fig. A-1. Instantaneous flow fields in the absence of hills.

For the sake of showing instantaneous flow fields in the nested grid system more clearly, the vertical slices at $x = -15L$, $-4L$, $0L$, and $4L$ are selected, with the $x = -15L$ slice in the coarse-grid domain, $x = -4L$ slice just downstream the fine-grid domain inlet, $x = 0L$ slice across the original point, and $x = 4L$ slice just upstream the fine-grid domain outlet. The streamwise vorticities, $\omega_x = \partial y/\partial z - \partial w/\partial x$, ranging from -10 s^{-1}–10 s^{-1} over these four spanwise slices are shown in Fig. A-2, where the buffering regions are sketched in blue. At $x = -15L$, only turbulences with large scales can be resolved by the coarse grid. These large-scale turbulences enter the fine-grid domain naturally, preserving the sizes of the structures, as clearly identified on the $x = -4L$ plane (Fig. A-2b). Furthermore, the transition effects in the spanwise direction are almost negligible. In the lateral buffering zones, a smooth refinement of turbulence structure is successfully reproduced without any obvious flow reflections.

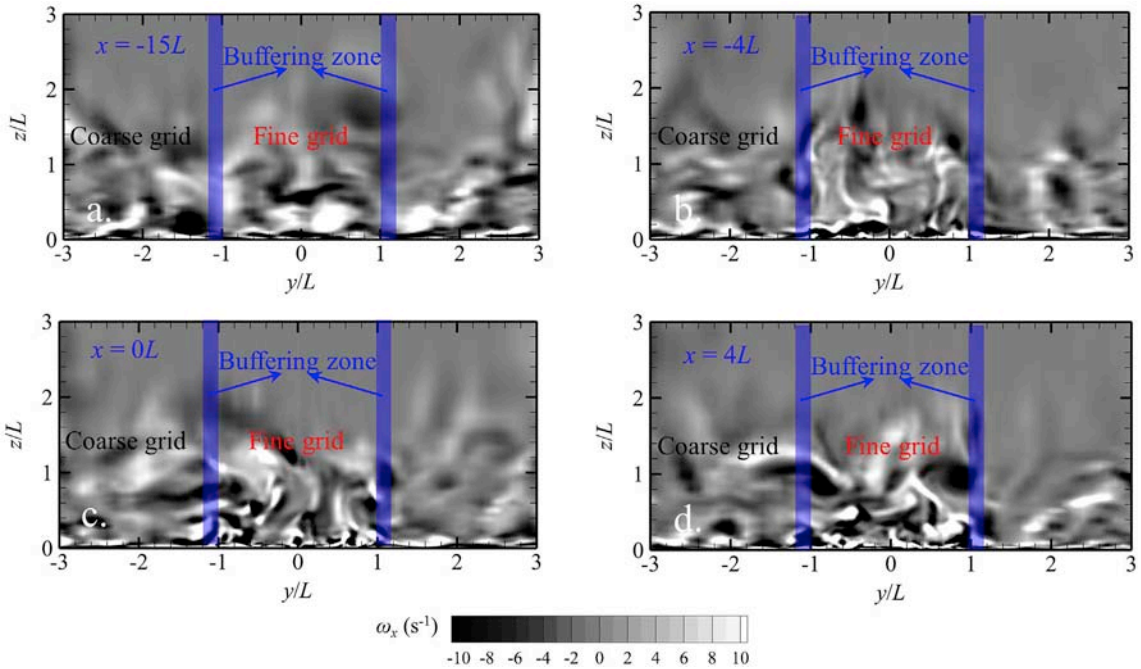

Fig. A-2. Contours of instantaneous streamwise vorticity on four vertical cross-sections: (a) $x = -15L$, (b) $x = -4L$, (c) $x = 0L$, and (d) $x = 4L$ in the absence of hills.

Fig. A-3 is a visualization of the flow fields by ω_y in the range of -10 s^{-1}–10 s^{-1} on the $y = 0$ slice with the presence of the topographies. The shaper contrast between the light and dark areas in the hill wakes implies that the vortex motions are more energetic for the higher hills. The turbulence structures around the hills are further analyzed through the instantaneous flow fields. After the iso-surfaces of Q-criteria are selected, the iso-surfaces of the normalized Q from 3.0 and -3.0 are visualized in Fig. A-7. The Q-criterion, $Q = 1/2(S_{ij}S_{ij} - \Omega_{ij}\Omega_{ij})$, quantifies the relative amplitude of the rotation rate and the strain rate of the flow (Dubief and Delcayre, 2000), where $S_{ij} = 1/2(\partial\tilde{u}_i/\partial x_j - \partial\tilde{u}_j/\partial x_i)$ and $\Omega_{ij} = 1/2(\partial\tilde{u}_i/\partial x_j + \partial\tilde{u}_j/\partial x_i)$ refer to the antisymmetric and symmetric components, respectively, of the velocity-gradient tensor.

The horseshoe-vortex structure approaching the upstream foothill is clear, which is enhanced as the hill slope increases, as shown in Fig. A-4. When

the summit is propagated over, the flow separates. In the wakes, the turbulence structures are organized in all the cases, whereas the organized structures become more energetic for steeper topographies. For the 3D hills, spiral structures are identified, as illustrated by the white dashed lines, and the pitches of the spirals narrow down as the hill slope increases. When the hill slope further increases to H8 (Fig. A-4 c), the spiral structures break down into separated circular tubes. These circular tubes are found to surround a major vortex core structure, identified by the yellow dashed line. From the animation of the flow fields, the circular tubes are observed to be generated at a frequency of about 0.8 L/u_∞, and the frequency of the wandering major core is about 0.05 L/u_∞. For the 2D ridges (Fig. A-4 d–e), the periodic wandering motion of the major vortex core structure is also found in R2, but this wandering motion disappears as the height increases to R4 and R8. For R4, a hairpin structure, identified by the white dashed lines, are found to be generated at a frequency of about 0.9 L/u_∞, whereas for R8, the hairpin structure disappears, and a vortex with a long spanwise size occurs periodically at a frequency of about 0.9 L/u_∞.

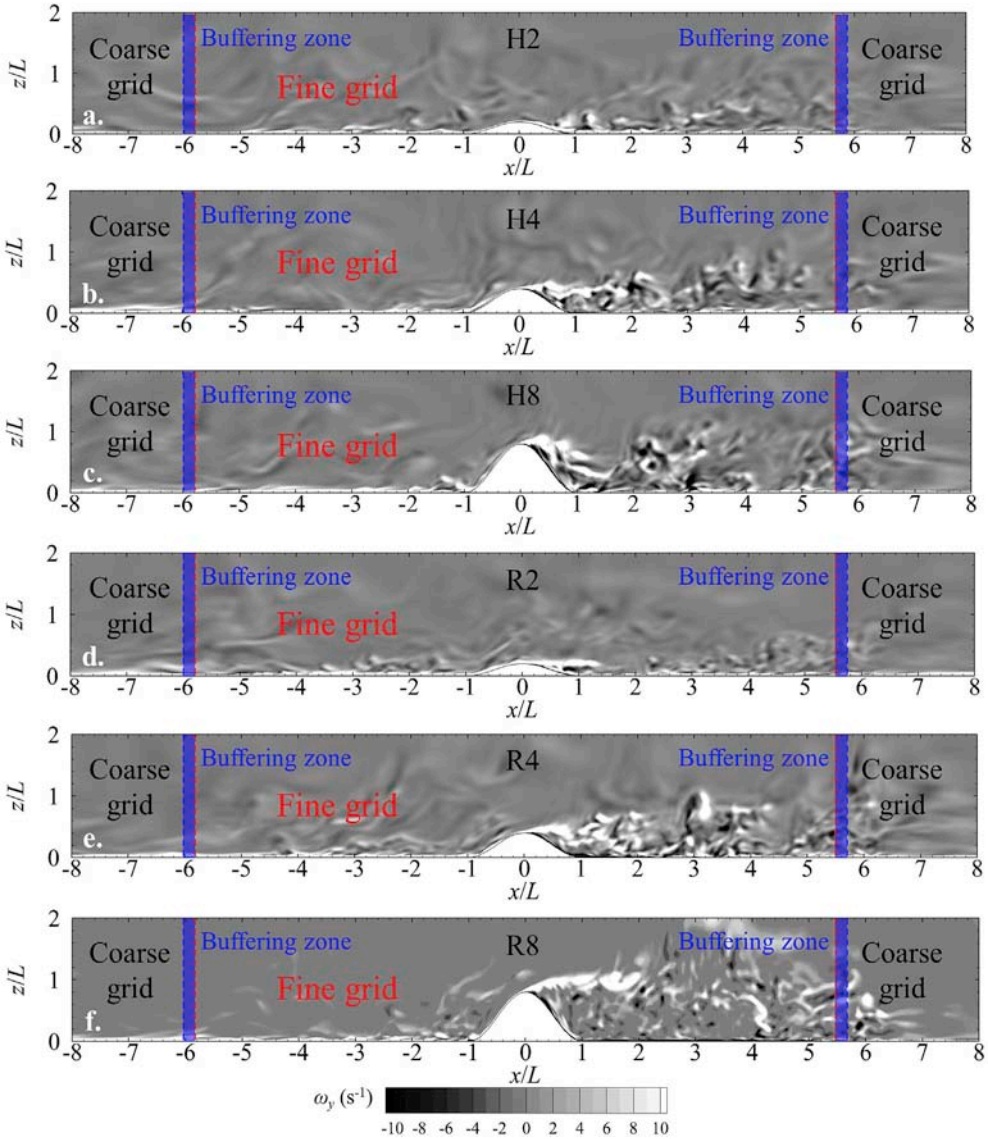

Fig. A-3. Contours of instantaneous spanwise vorticity on $y = 0$ slice in the presence of hills (a) H2, (b) H4, (c) H8, (d) R2, (e) R4, and (f) R8.

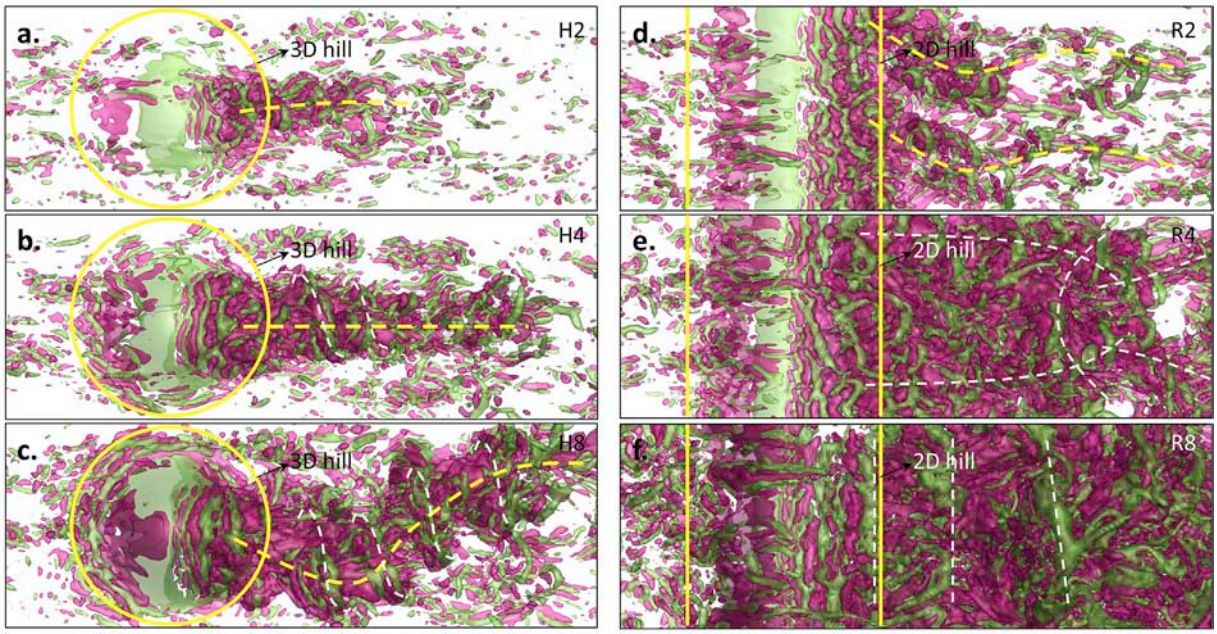

Fig. A-4. Instantaneous flow fields visualized by Q-criteria, for (a) H2, (b) H4, (c) H8, (d) R2, (e) R4, and (f) R8, from top view. The dashed yellow lines indicate the vortex structures with low frequency, and the white dashed lines indicate the vortex structures with high frequencies. Same snapshots as Fig. A-3.

Moreover, the reattachment of the flow downstream of H8 seems shorter than that of R8, which will be more evidently presented by the streamlines on the $y = 0$ plane, as shown in Fig. A-5, where much denser sources below $z = L$, and additional ones in the near-wake regions are introduced to provide detailed information about the flows surrounding the topographies. The blue lines represent the center of the recirculating bubble, which is the connection of the positions with mean streamwise velocity $u = 0$. For H2 and R2, the distortions of the streamlines caused by the topographies are negligible on the windward sides. Similar behaviors are also observed for H4 and R4. However, for H8 and R8, stagnation points at ($x = -0.8L$, $y = 0.1L$ for H8, and $x = -0.6L$, $y = 0.1L$ for R8) occur, leading to horseshoe vortices and abrupt increases in velocity fluctuations. Moving downstream, the flow separates, and with the increase in h, the separation point slightly shifts upstream to locations $x = 0.21L$, $0.12L$, $0.03L$, 0.20, 0.12, and 0.02 in H2, H4, H8, R2, R4, and R8, respectively. In addition, the flow reattaches at $x = 0.8L$, $1.1L$, $1.4L$, $0.8L$, $2.4L$, and $5.1L$ in H2, H4, H8, R2, R4, and R8, respectively. Therefore, we can say that the reattachment of the flow will become difficult as the slope increases or as the shape changes from 3D hill to 2D ridge. In addition, the differences of the flow fields between the 3D hills and the 2D ridges will become more evident as the slopes increase. It is also noteworthy that the streamlines starting from the summit are consistently flattened because of the presence of separation bubble regardless of the slope or the hill shape, whereas the flows appear to move gently upward just behind the summit in H8 and R8.

Finally, a small secondary recirculation near the crest is identified, as shown in Fig. A-6. Interestingly, this counterclockwise-rotating structure exists irrespective of the steepness or hill shape, and the length and position of this rotating structure do not vary considerably when the slope rises. However, if the shape of the topography is changed from 3D hill to 2D ridge, the thickness of the secondary bubble will become thinner. The secondary recirculation bubble has a very small height, less than $0.005L$, in the vertical direction, and thus to reproduce this secondary recirculation bubble, the grids near the wall should be fine enough. If the grid height attaching the hill surface cannot resolve the large gradient of wind velocity near surface, the law-of-the-wall principle will be applied, and as a result, the shear stress on the hill surface cannot be predicted well. In the present simulations, the $z+$ value is less than 1 in all of the cases.

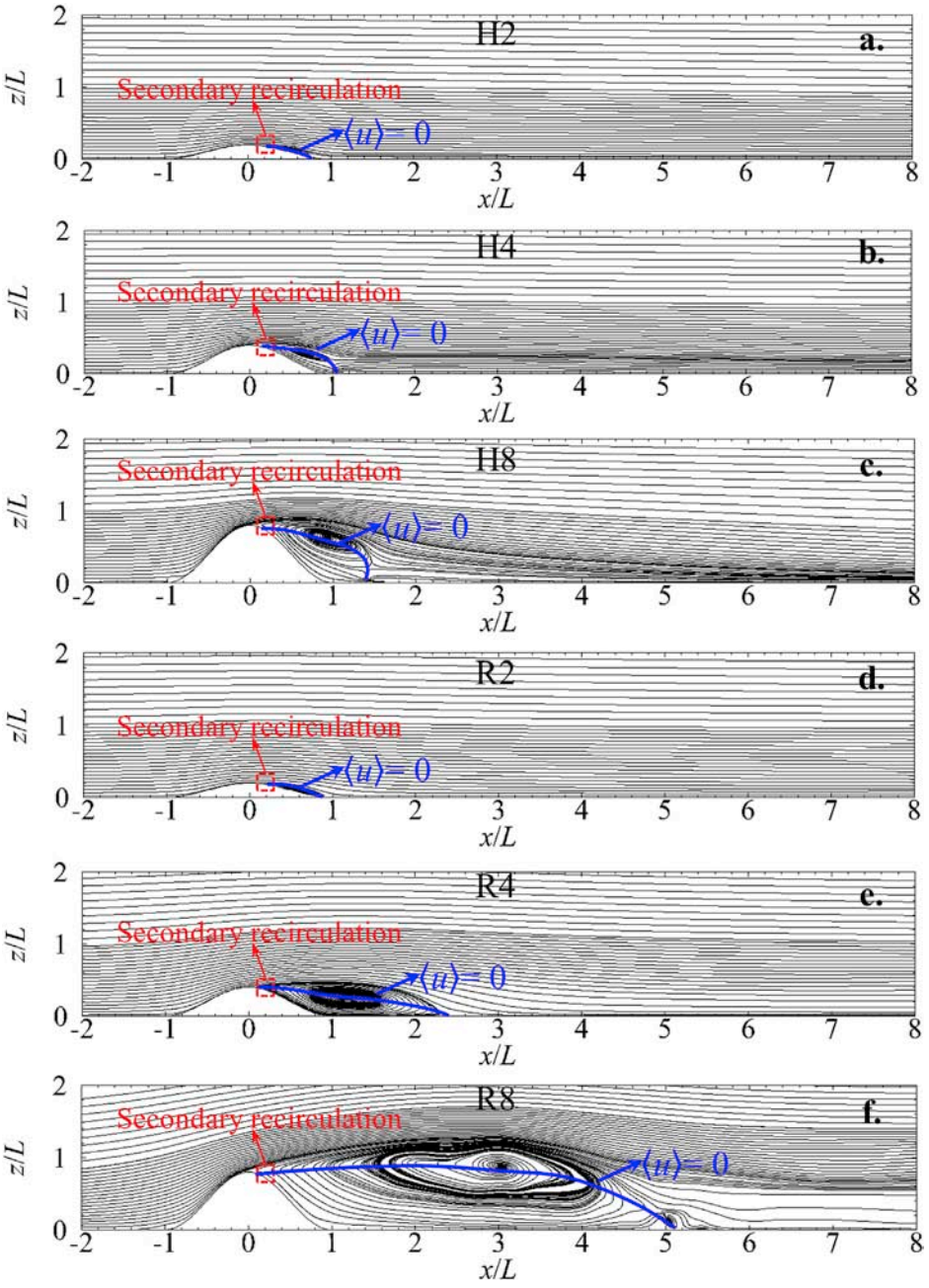

Fig. A-5. Streamlines on the $y = 0$ slice: (a) H2, (b) H4, (c) H8, (d) R2, (e) R4, and (f) R8.

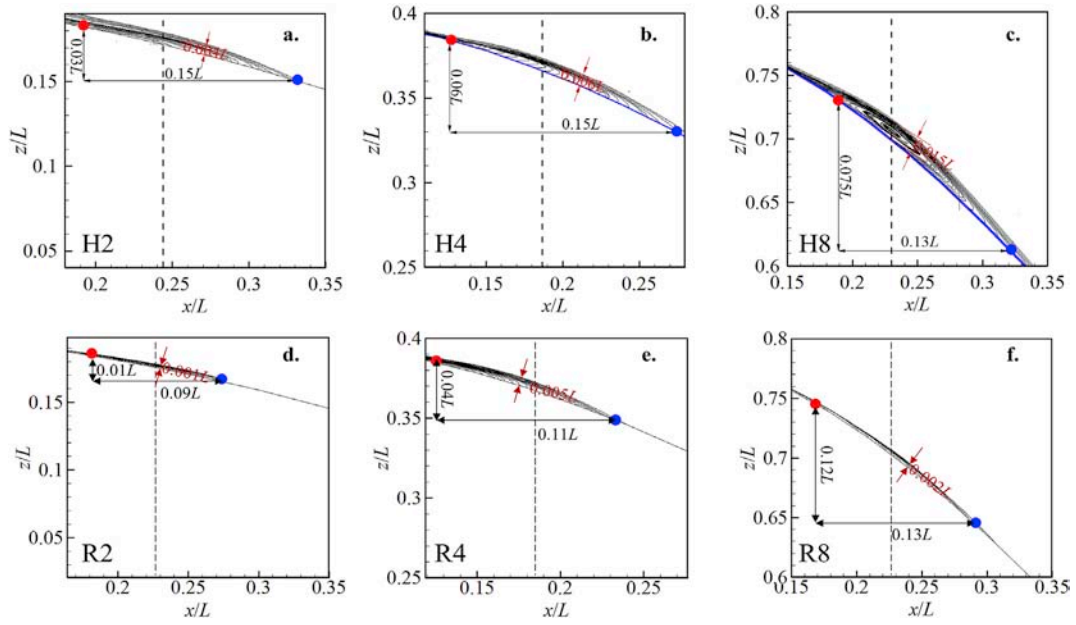

Fig. A-6. Illustration of secondary recirculation: (a) H2, (b) H4, (c) H8, (d) R2, (e) R4, and (f) R8.

Appendix-2: Proposed analytical model for fractional speed-up ratio

Fractional speed-up ratio is broadly applied to assess the effects of topography on the wind speed. ΔS is defined as follows: $\Delta S = \Delta u / u_0 = [u(x, z') - u_0(z')]/u_0(z')$, where $u(x, z')$ denotes the streamwise velocity at height z', and $u_0(z')$ is the reference streamwise velocity at the same height in the absence of topography. An analytical model was developed by Taylor and Lee (1984) based on the linear theory raised by Jackson and Hunt (1975), expressed as

$$\Delta S_{max} = Bh/L \text{ and } \Delta S = \Delta S_{max} e^{-Az'/L} \tag{A-1}$$

where the constants A and B equal 4.0 and 1.6, respectively, for a 3D hill, and equal 3.0 and 2.0, respectively, for a 2D ridge. Here, the predicted ΔS at $x = 0$ from the present LES and those from the analytical model are depicted in Fig. A–7. Apparently, the speed-up of the wind is enhanced when the 3D hill turns steeper, reaching around 0.7 for H8 near the ground, whereas ΔS from the analytical model by Taylor and Lee (1984) is roughly twice as large as the corresponding LES prediction. For the 2D ridges, ΔS is almost a constant, with its value scattering at around 0.5, and for R8, ΔS from the analytical model by Taylor and Lee (1984) is roughly three times as large as the corresponding LES prediction.

Taylor and Lee (1984) commented that this model can be adopted only when the maximum slope is less than 0.3. If the maximum slope is larger than 0.3, the linear theory based on the assumption that there is no separation of flows over hills will not work. In the present study, the maximum slopes for all of the cases are larger than the upper limitation of the Taylor model, which is a reason for the discrepancies between LES and the analytical model by Taylor and Lee (1984). Based on the information available from LES, an analytical model for both the 3D hills and the 2D ridges are proposed by fitting the LES data. The basic form of the formulations is similar to those by Taylor and Lee (1984). For 3D hills, when the slope is larger than 0.3, the analytical model is formulated as

$$\Delta S = \left(\frac{Bh}{L} + C\right) e^{-Az'/L} + D \cdot E^{-Az'/L}, \quad where,\ A = 7.0,\ B = 0.9,\ C = 0.24,\ D = 0.15,\ E = 1.1 \tag{A-2}$$

For 2D hills, when the slope is larger than 0.3, the analytical model is formulated as

$$\Delta S = \left(\frac{Bh}{L} + C\right) e^{-Az'/L} + D \cdot E^{-Az'/L}, \quad where,\ A = 7.0,\ B = 0.1,\ C = 0.45,\ D = 0.15,\ E = 1.1 \tag{A-3}$$

In Eq. (A-2 and 3), the constants A, B, C, D, and E are determined by fitting the profiles in the present simulations using least square method. Comparing the data in LES, the analytical model by Taylor and Lee (1984), and the proposed model in the present study, we can find that the proposed model shows clear improvement and satisfactory consistency with respect to LES.

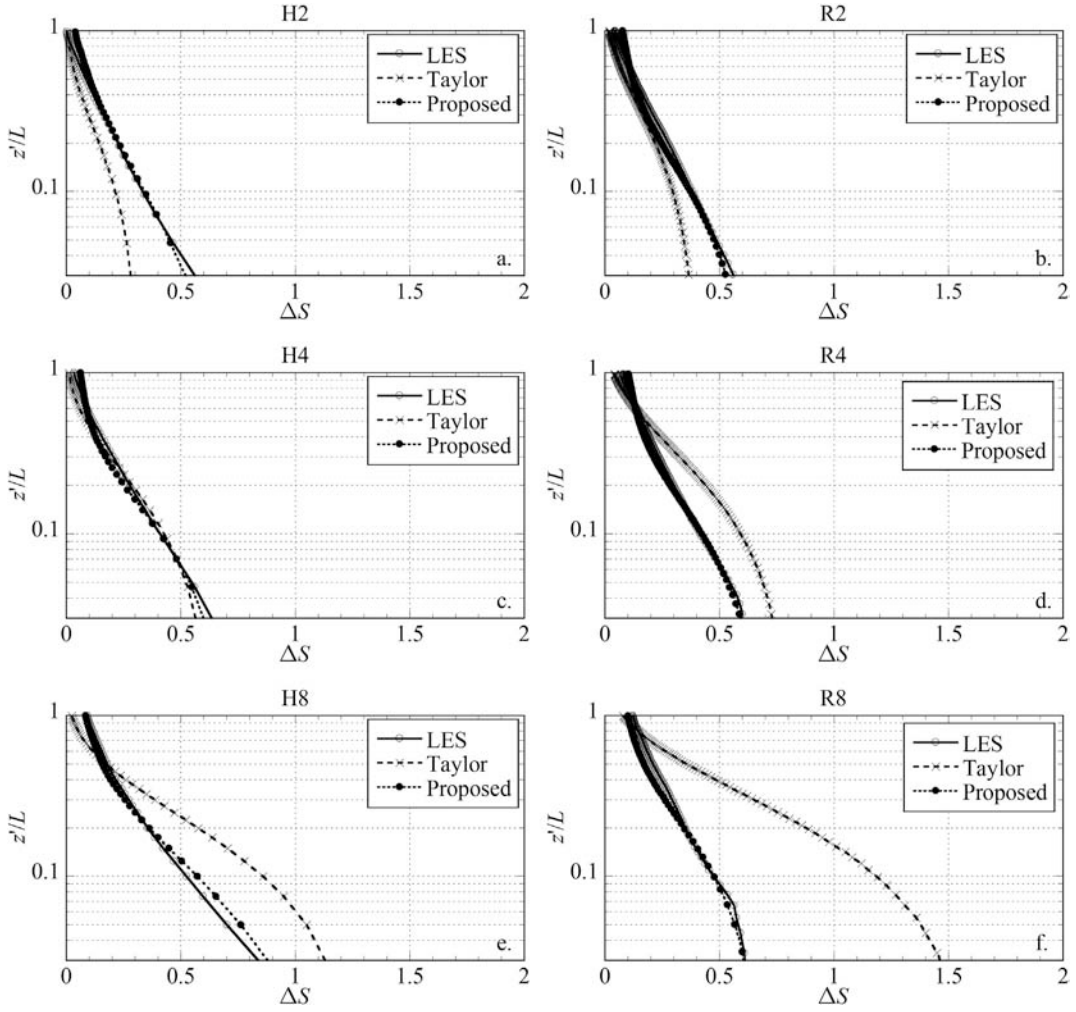

Fig. A–7. Vertical profiles of fractional speed-up ratio at the hill top, (a) H2, (b) H4, (c) H8, (d) R2, (e) R4, and (f) R8.

References

Apsley, D., Castro, P., 1997. Flow and dispersion over hills: comparison between numerical predictions and experimental data. J. Wind Eng. Ind. Aerod. 67, 375–386.

Balogh, M., Parente, A., Benocci, C., 2012. RANS simulation of ABL flow over complex terrains applying an enhanced *k-ε* model and wall function formulation. J. Wind Eng. Ind. Aerod. 104–106, 360–368.

Balogh, M., Parente, A., 2015. Realistic boundary conditions for the simulation of atmospheric boundary layer flows using an improved *k-ε* model. J. Wind Eng. Ind. Aerod. 144, 183–190.

Cao, S., Tamura, T., 2006. Experimental study on roughness effects on turbulent boundary layer flow over a two-dimensional steep hill. J. Wind Eng. Ind. Aerod. 94 (1), 1–19.

Cao, S., Tamura, T., 2007. Effects of roughness blocks on atmospheric boundary layer flow over a two-dimensional low hill with/without sudden roughness change. J. Wind Eng. Ind. Aerod. 95 (8), 679–695.

Cao, S., Wang, T., Ge, Y., Tamura, Y., 2012. Numerical study on turbulent boundary layers over two-dimensional hills - effects of surface roughness and slope. J. Wind Eng. Ind. Aerod. 104–106, 342–349.

Carpenter, P., Locke, N., 1999. Investigation of wind speeds over multiple two-dimensional hills. J. Wind Eng. Ind. Aerod. 83 (1), 109–120.

Chang, C., Schmidt, J., Dörenkämper, M., Stoevesandt, B., 2018. A consistent steady state CFD simulation method for stratified atmospheric boundary layer flows. J. Wind Eng. Ind. Aerod. 172, 55–67.

Coppin, P., Bradley, E., Finnigan, J., 1994. Measurements of flow over an elongated ridge and its thermal stability dependence: the mean field. Boundary-Layer Meteorol. 69 (1–2), 173–199.

Dubief, Y., Delcayre, F., 2000. On coherent-vortex identification in turbulence. J. Turbul. 1 (11), 1–20.

Ferreira, A., Lopes, A., Viegas, D., Sousa, A., 1995. Experimental and numerical simulation of flow around two-dimensional hills. J. Wind Eng. Ind. Aerod. 54–55, 173–181.

GarcÍA-Villalba, M., Li, N., Rodi, W., Leschziner, M.A., 2009. Large-eddy simulation of separated flow over a three-dimensional axisymmetric hill. J. Fluid Mech. 627, 55–96.

Germano, M., Piomelli, U., Moin, P., Cabot, W.H., 1991. A dynamic subgrid-scale eddy viscosity model. Phys. Fluids A3 (7), 1760–1765.

Gong, W., Ibbetson, A., 1989. A wind tunnel study of turbulent flow over model hills. Boundary-Layer Meteorol. 49 (1), 113–148.

Griffiths, A.D., Middleton, J.H., 2010. Simulations of separated flow over two-dimensional hills. J. Wind Eng. Ind. Aerod. 98 (3), 155–160.

Hu, P., Li, Y., Han, Y., Cai, S., Xu, X., 2016. Numerical simulations of the mean wind speeds and turbulence intensities over simplified gorges using the SST *k-ω* turbulence model. Eng. Appl. Comp. Fluid. 10 (1), 361–374.

Hunt, J., Carruthers, D., 1990. Rapid distortion theory and the 'problems' of turbulence. J. Fluid Mech. 212, 497–532.

Hunt, J., Snyder, W., 1980. Experiments on stably and neutrally stratified flow over a model three-dimensional hill. J. Fluid Mech. 96 (4), 671–704.

Iizuka, S., Kondo, H., 2004. Performance of various sub-grid scale models in large-eddy simulations of turbulent flow over complex terrain. Atmos. Environ. 38 (40), 7083–7091.

Iizuka, S., Kondo, H., 2006. Large-eddy simulations of turbulent flow over complex terrain using modified static eddy viscosity models. Atmos. Environ. 40 (5), 925–935.

Inagaki, M., Kondoh, T., Nagano, Y., 2005. A mixed-time-scale SGS model with fixed model-parameters for practical LES. J. Fluid Eng.-T. ASME 127, 1–13.

Ishihara, T., Hibi, K., Oikawa, S., 1999. A wind tunnel study of turbulent flow over a three-dimensional steep hill. J. Wind Eng. Ind. Aerod. 83 (1), 95–107.

Ishihara, T., Hibi, K., 2000. Numerical simulation of turbulent flow over a steep hill. J. Wind Eng. 83, 175–188.

Ishihara, T., Fujino, Y., Hibi, K., 2001. A wind tunnel study of separated flow over a two-dimensional ridge and a circular hill. J. Wind Eng. 89, 573–576.

Jackson, P., Hunt, J., 1975. Turbulent wind flow over a low hill. Q. J. Roy. Meteorol. Soc. 101 (430), 929–955.

Kay, S., Marple, S., 1981. Spectrum analysis: a modern perspective. Proc. IEEE 69, 1380–1419.
Kim, H., Lee, C., Lim, H., Kyongb, N., 1997. An experimental and numerical study on the flow over two-dimensional hills. J. Wind Eng. Ind. Aerod. 66, 17–33.
Kolmogorov, A., 1941. Dissipation of energy in locally isotropic turbulence. Akademiia Nauk Sssr Doklady 32 (1890), 15–17.
Kim, J., Baik, J., Chun, H., 2001. Two-dimensional numerical modeling of flow and dispersion in the presence of hill and buildings. J. Wind Eng. Ind. Aerod. 89 (10), 947–966.
Kobayashi, M., Pereira, J., Siqueira, M., 1994. Numerical study of the turbulent flow over and in a model forest on a 2D hill. J. Wind Eng. Ind. Aerod. 53 (3), 357–374.
Li, J., 1987. Classification of fundamental types of geomorphological form in China. Geogr. Res. 6 (2), 32–39 (In Chinese).
Li, Q., Maeda, T., Kamada, Y., Yamada, K., 2017. Experimental investigation of flow over two-dimensional multiple hill models. Sci. Total Environ. 609, 1075–1084.
Liu, Z., Ishihara, T., He, X., Niu, H., 2016. LES study on the turbulent flow fields over complex terrain covered by vegetation canopy. J. Wind Eng. Ind. Aerod. 155, 60–73.
Liu, Z., Ishihara, T., Tanaka, T., He, X., 2016. LES study of turbulent flow fields over a smooth 3-D hill and a smooth 2-D ridge. J. Wind Eng. Ind. Aerod. 153, 1–12.
Loureiro, J., Soares, D., Fontoura Rodrigues, J., Pinho, F., Silva, A., 2007a. Water tank and numerical model studies of flow over steep smooth two-dimensional hills. Boundary-Layer Meteorol. 122 (2), 343–365.
Loureiro, J., Pinho, F., Silva, A., 2007. Near wall characterization of the flow over a two-dimensional steep smooth hill. Exp. Fluid 42, 441–457.
Loureiro, J., Alho, A., Silva, A., 2008. The numerical computation of near-wall turbulent flow over a steep hill. J. Wind Eng. Ind. Aerod. 96 (5), 540–561.
Lubitz, W., White, B., 2007. Wind-tunnel and field investigation of the effect of local wind direction on speed-up over hills. J. Wind Eng. Ind. Aerod. 95 (8), 639–661.
Lun, Y., Mochida, A., Murakami, S., Yoshino, H., Shirasawa, T., 2003. Numerical simulation of flow over topographic features by revised k-ε models. J. Wind Eng. Ind. Aerod. 91 (1–2), 231–245.
Ma, Y., Liu, H., 2017. Large-eddy simulations of atmospheric flows over complex terrain using the immersed-boundary method in the weather research and forecasting model. Boundary-Layer Meteorol. 165 (3), 421–445.
Mello, P., Yanagihara, J., 2010. Numerical prediction of gas concentrations and fluctuations above a triangular hill within a turbulent boundary layer. J. Wind Eng. Ind. Aerod. 98 (2), 113–119.
Meneveau, C., Lund, T.S., Cabot, W.H., 1996. A Lagrangian dynamic subgrid-scale model for turbulence. J. Fluid Mech. 319, 353–385.
Mickle, R., Cook, N., Hoff, A., Jensen, N., Salmon, J., Taylor, P., Tetzlaff, G., Teunissen, H., 1988. The Askervein hill project: vertical profiles of wind and turbulence. Boundary-Layer Meteorol. 43 (1–2), 143–169.
Neff, D., Meroney, R., 1998. Wind-tunnel modeling of hill and vegetation influence on wind power availability. J. Wind Eng. Ind. Aerod. 74–76, 335–343.
Paiva, S., Bodstein, R., Menezes, F., 2009. Numerical simulation of atmospheric boundary layer flow over isolated and vegetated hills using RAMS. J. Wind Eng. Ind. Aerod. 97 (9–10), 439–454.
Pieterse, E., Harms, M., 2013. CFD investigation of the atmospheric boundary layer under different thermal stability conditions. J. Wind Eng. Ind. Aerod. 121 (5), 82–97.
Press, W., Teukolsky, S., Vetterling, W., 2007. Numerical Recipes 3rd Edition: the Art of Scientific Computing. Cambridge University Press, pp. 681–685.
Salmon, J., Bowen, A., Hoff, A., Johnson, R., Mickle, R., Taylor, P., Tetzlaff, G., Walmsley, J., 1988. The Askervein hill project: mean wind variations at fixed heights above ground. Boundary-Layer Meteorol. 43 (3), 247–271.
Sajjadi, S., Craft, T., Feng, Y., 2001. A numerical study of turbulent flow over a two-dimensional hill. Int. J. Numer. Methods Fluid. 35 (1), 1–23.
Smagorinsky, J., 1963. General circulation experiments with the primitive equations. I. The basic experiment. Month. Wea. Rev. 91, 99–164.
Takahashi, T., Ohtsu, T., Yassin, M., Kato, S., Murakami, S., 2002. Turbulence characteristics of wind over a hill with a rough surface. J. Wind Eng. Ind. Aerod. 90 (12), 1697–1706.
Takahashi, T., Kato, S., Murakami, S., Ooka, R., Yassin, F., Kono, R., 2005. Wind tunnel tests of effects of atmospheric stability on turbulent flow over a three-dimensional hill. J. Wind Eng. Ind. Aerod. 93 (2), 155–169.
Tamura, T., Okuno, A., Sugio, Y., 2007. LES analysis of turbulent boundary layer over 3D steep hill covered with vegetation. J. Wind Eng. Ind. Aerod. 95 (9), 1463–1475.
Tamura, T., Cao, S., Okuno, A., 2007b. LES study of turbulent boundary layer over a smooth and a rough 2D hill model. Flow, Turbul. Combust. 79 (4), 405–432.
Taylor, A., Lee, J., 1984. Simple Guidelines for estimating wind speed variations due to small scale topographic features. Climatological Bull 18 (2), 3–22.
Uchida, T., Ohya, Y., 1997. A numerical study of stably stratified flows over a two-dimensional hill - Part I. free-slip condition on the ground. J. Wind Eng. Ind. Aerod. 67–68 (4), 493–506.